THE ASTROPHYSICAL JOURNAL, 430:467–494, 1994 August 1

SUPERLUMINAL MOTION STATISTICS AND COSMOLOGY

R. C. VERMEULEN AND M. H. COHEN
Owens Valley Radio Observatory, Mail Code 105-24, California Institute of Technology, Pasadena, CA 91125;
rcv@astro.caltech.edu,mhc@deimos.caltech.edu
Received 1993 July 30; accepted 1993 October 25

ABSTRACT

This paper has three parts. First, we give an up-to-date overview of the available apparent velocity (β_{app}) data; second, we present some statistical predictions from simple relativistic beaming models; third, we discuss the inferences which a comparison of data and models allows for both relativistic jets and cosmology.

We demonstrate that, in objects selected by Doppler-boosted flux density, likely Lorentz factors (γ) can be estimated from the first-ranked β_{app} in samples as small as 5. Using 25 core-selected quasars, we find that *the dependence of γ on redshift differs depending on the value of q_0*: γ is close to constant over z if $q_0 = 0.5$, but increases with z if $q_0 = 0.05$. Conversely, this result could be used to constrain q_0, using either theoretical limits on γ or observational constraints on the full distribution of γ in each of several redshift bins, as could be derived from the β_{app} statistics in larger samples.

We investigate several modifications to the simple relativistic beam concept, and their effects on the β_{app} statistics. There is likely to be a spread of γ over the sample, with relative width W. There could also be a separate pattern and bulk γ, which we model with a factor $r \equiv \gamma_p/\gamma_b$. The values of W and r are coupled, and a swath in the (W, r)-plane is allowed by the β_{app} data in core-selected quasars. Interestingly, γ_p could be both smaller and larger than γ_b, or they could be equal, if W is large, but *the most naive model* (0, 1)*—the same Lorentz factor in all sources and no separate pattern motions—is excluded.*

A possible cutoff in quasar jet orientations, as in some unification models, causes a sharp shift toward higher β_{app} in randomly oriented samples but does not strongly affect the statistics of core-selected samples. If there is moderate bending of the jets on parsec scales, on the other hand, this has no significant impact on randomly oriented samples, but it can have surprisingly varied results in core-selected quasars.

It could be that individual jets incorporate a broad range of γ, but that only one value is observed per jet, as given by Doppler favoritism. The β_{app} statistics in core-selected quasars are a poor indicator of any such internal range. Furthermore, at small angles to the line of sight, Doppler favoritism is actually not a good γ-selection mechanism. However, for randomly oriented samples, such as lobe-selected quasars, the effects of an internal range of γ can be confused with the angle cutoff in unification scenarios. This might greatly complicate using β_{app} in lobe-selected quasars either to constrain such unification models or to determine the cosmological parameters H_0 and q_0.

Subject headings: cosmology: observations — galaxies: jets — quasars: general — radio continuum: galaxies — relativity — techniques: interferometric

1. INTRODUCTION

Many active galactic nuclei (AGNs) contain compact radio sources with several components which appear to move apart in successive high-resolution (VLBI) images. When the apparent transverse velocity of separation exceeds the speed of light ($\beta_{app} \equiv v/c > 1$), the motion, and the object, are called superluminal. Superluminal motion has now been observed in dozens of sources, and is therefore no longer rare in an absolute sense. However, it is just becoming feasible to analyze the β_{app} distribution in well-defined source categories. With the imminent availability of the Very Long Baseline Array (VLBA) for large-scale routine observing, this is an appropriate time to review the currently available database and its implications, as well as to indicate how a substantial increase in the number of measured velocities could be used to derive important constraints for relativistic jet astrophysics, for unification models, and for cosmology.

The popular kinematic explanation for superluminal motion is that the nuclear region contains a narrow, nearly straight, expanding jet of plasma in relativistic motion. If the jet is pointed close to the line of sight, contraction of the apparent timescale can give rise to superluminal motion. It also produces Doppler boosting, which brings relatively large numbers of these objects into the strong-source catalogs. Superluminal sources have been studied for over two decades, and their main observational properties are now well established (for recent reviews see, e.g., Porcas 1987; Zensus & Pearson 1988). They expand and do not contract, and from time to time new components emerge from the core. Note, however, that it has generally been impossible to register VLBI maps on the sky (but see Bartel et al. 1986), so that only relative motions, or the absence of motion between components, can be measured. Many observations are consistent with uniform outward motion, independent of wavelength. However, a few instances of acceleration and deceleration have been observed, and evidence has come to light that the motion can be along a bent but stable track (Zensus, Cohen, & Unwin 1994). A thorough understanding of the astrophysical processes underlying these phenomena remains elusive, and we will not review current models here. However, as we will show, with almost purely kinematic arguments, superluminal motion statistics is beginning to address important issues such as the distribution of

Lorentz factors and whether or not the observed transverse motions of the components (patterns) are similar in magnitude to the bulk motion in the jets.

Superluminal motion statistics can potentially be used to test so-called unification models which hold that quasars and Fanaroff-Riley Class II (FR II) radio galaxies are similar objects intrinsically, and that they form a sequence with increasing jet inclination to the line of sight (e.g., Orr & Browne 1982; Scheuer 1987; Barthel 1989). They predict that the highest β_{app} should be found in core-dominated quasars, with lower values in the lobe-dominated quasars, and even lower values in FR II galaxies. It is possible that the higher luminosity BL Lacertae objects belong in the same sequence and have their jets pointed almost directly at the observer, yielding predominantly low β_{app}. Similar unification models have also been suggested for lower luminosity BL Lac objects and FR I radio galaxies (for a discussion of this issue see, e.g., Impey, Lawrence, & Tapia 1991; Urry, Padovani, & Stickel 1991; Padovani 1992; Bicknell 1994).

Attempts have been made to use superluminal sources for cosmological studies, since they allow distant (old) regions to be studied directly, without intermediate calibrators. The most direct "standard" relative transverse velocity ($2c$) would be obtained between any two relativistically moving components in oppositely directed jets, if the jets are not pointed close to the line of sight (e.g., Pelletier & Roland 1990). Unfortunately, no clear two-sided superluminals have yet been found; Doppler beaming may well be responsible for this. Lynden-Bell (1977) and Ekers & Liang (1990) have discussed a light-echo superluminal motion model, in which there is no Doppler boosting to bias the angular distribution of the observed sources, despite other evidence in favor of Doppler boosting. Cohen et al. (1988) summarized the internal proper motion data then available in a "μ-z diagram" (Yahil 1979). They used the simple relativistic beaming model, and showed that the upper μ envelope decreased with z in a way which is consistent with Friedmann cosmology and inconsistent with several other models. This analysis indicated that if superluminal velocities represent bulk motion, then substantial Lorentz factors ($\gamma_b >$ 10) are needed at least in some cases.

Throughout this paper standard Friedmann cosmology is used. No a priori value for the deceleration parameter (q_0) is assumed; in fact, it will be shown that the statistics of superluminal velocities may be used as a tool to determine q_0. We will use $q_0 = 0.05$ and $q_0 = 0.5$ to demonstrate how the difference between an open and a closed universe affects superluminal motion statistics. Where possible, quantities involving Hubble's constant are given in terms of h, with $H_0 = 100$ km s^{-1} Mpc^{-1}. When a specific choice is unavoidable, $h = 0.6$ is used.

This paper has three main parts. Some of our results are extension of work presented earlier by Cohen & Vermeulen (1992). First, in § 2, we give a detailed up-to-date compilation of the VLBI multiepoch internal proper motion measurements published to date. We define a number of source categories, and briefly discuss differences in their superluminal motion statistics. Second, in § 3, we outline several variants of the simple relativistic beaming model, applicable for different source categories, and we show the predicted β_{app} distributions. We then demonstrate how these change if there are separate pattern velocities, if the jets are bent, or if there is a restricted range of angles to the line of sight. The models also show the potential utility of the β_{app} upper envelope in very small samples. In the third part of the paper, we use the model results to interpret the observed β_{app} distributions in lobe-selected and core-selected quasars. For the lobe-selected quasars (§ 4), we comment mainly on the potential use in constraining unification models. For the core-selected quasars (§ 5), we first discuss bulk and pattern Lorentz factors, and jet bending, by studying the full β_{app} range without regard for source redshift. Then we analyze the upper β_{app} envelope as a function of redshift; it is intriguingly different for different values of q_0. We indicate how a future study of the β_{app} distribution as a function of redshift might be used to constrain the geometry of the universe. Finally, § 6 is a summary of our results.

2. COMPILATION OF PROPER MOTIONS

2.1. *The Data*

Table 1 lists the 66 extragalactic sources for which we have been able to find multiepoch VLBI internal proper motion observations in the literature, or for which we are currently preparing a paper. We did not include sources in which the occurrence of superluminal motion has been argued based only on variability or on the timing of a flux outburst. Likewise, lower velocity limits based only on the nonexistence of a component at an earlier epoch have not been included in Table 1. This is a superset of the list published by Cohen et al. (1988), and contains more than twice as many sources. With four exceptions, Table 1 also contains all of the sources in recent lists by Porcas (1987), Mutel (1990), and Ghisellini et al. (1993), as well as additional objects. The exceptions are 0235+164 (e.g., Bååth 1984; Mutel 1990), which is essentially unresolved on milliarcsecond scales but has been argued to be superluminal based only on variability; 1807+698 (3C 371), which has no clear moving features (T. J. Pearson 1993, private communication) but again was argued to be superluminal based on variability (Lind 1987); 1845+797 (3C 390.3), where ambiguous component identifications, discussed by Alef et al. (1988), have now been resolved with the result that there is no clear motion (T. J. Pearson 1993, private communication); and 2134+004 (Pauliny-Toth et al. 1990), in which we believe the rapid morphological variability cannot (yet?) be linked to relative motion of definable components. Further intensive monitoring of such sources may reveal whether they have recognizable motion or whether they show different phenomena. Note that we have taken all internal proper motions from the original references, and have kept different measurements (e.g., of different components) separate whenever possible; this accounts for quite a few differences with the aforementioned lists.

The redshifts (col. [3]) were mostly taken from Véron-Cetty & Véron (1991) and verified in Hewitt & Burbidge (1991); in case of significant disagreements ($\Delta z > 0.001$), or when sources were not listed, the original publications were consulted. Note 4 indicates new redshifts, supplied by C. R. Lawrence (1993, private communication). The redshifts for 1228+127 (M87) and 1322−472 (Cen A) do not correspond to actual emission-line spectra but were computed assuming $h = 0.6$ and distances of 16 and 4 Mpc, respectively. Apart from the empty-field object 0355+508 (NRAO 150), all sources have been classified in column (4) as one of three types: Q = quasar, G = galaxy, or B = BL Lac object. Further possible designations for quasars are c = core-selected, l = lobe-selected, or p = compact-symmetric. These classifications are discussed in § 2.3.

Columns (5)–(8) list the measurements of internal proper

TABLE 1

COMPILATION OF INTERNAL PROPER MOTIONS

IAU Name (1)	Common Name (2)	z (3)	Classification (4)	Component ID (5)	Observation Wavelength (cm) (6)	Number of Epochs (7)	Proper Motion μ (mas yr^{-1}) (8)	Reliability (9)	$\beta_{app} h$ $q_0 = 0.05$ (10)	$\beta_{app} h$ $q_0 = 0.5$ (11)	References (12)	Notes (13)
0016+731	...	1.781	Qc	...	6	2	0.22 ± 0.053	1	11.87 ± 2.86	8.35 ± 2.01	1	1, 2
0055+301	NGC 315	0.0167	G	B	6, 3	2	<0.7	1	<0.55	<0.55	2	3
0106+013	...	2.107	Qc	C2	6	3	0.20 ± 0.05	2	12.26 ± 3.07	8.20 ± 2.05	3	
0108+388	...	0.67	Qp	...	6	3	<0.10	1	<2.49	<2.14	4	4, 5
0133+207	3C 47	0.425	Ql	K	3	2	0.24 ± 0.05	1	4.06 ± 0.85	3.69 ± 0.77	5	
0153+744	...	2.338	Qc	C2	6	3	0.02 ± 0.04	3	1.33 ± 2.65	0.86 ± 1.72	6	
				C3	6	2	0.08 ± 0.22	1	5.30 ± 14.58	3.43 ± 9.44	6	
				C4*	6	2	−0.12 ± 0.22	1	−7.96 ± 14.58	−5.15 ± 9.44	6	
0212+735	...	2.367	Qc	C2*	6	3	0.09 ± 0.05	2	6.02 ± 3.35	3.88 ± 2.16	6	
				C3	6	2	0.07 ± 0.19	1	4.68 ± 12.71	3.02 ± 8.19	6	
				C4	6	2	−0.14 ± 0.29	1	−9.37 ± 19.40	−6.04 ± 12.51	6	
0234+285	...	1.207	Qc	...	6	2	0.3 ± 0.15	1	11.98 ± 5.99	9.29 ± 4.65	7	6, 7
0316+413	3C 84	0.017	G	K1	1	8	0.54 ± 0.12	3	0.43 ± 0.10	0.43 ± 0.10	8	8
0333+321	NRAO 140	1.263	Qc	B	3	2	0.15 ± 0.01	2	6.21 ± 0.41	4.77 ± 0.32	9	9, 10
0355+508	NRAO 150	...	...	...	4	3	0 ± 0.05	1	...	...	10	11
0415+379	3C 111	0.0485	G	...	6	2	1.54 ± 0.2	1	3.45 ± 0.45	3.42 ± 0.44	11	12, 13
0430+052	3C 120	0.033	G	A	6, 3	4	1.35	2	2.08	2.06	12	14, 15
				B*	6, 3	7	2.53	3	3.89	3.86	12	14, 15
				C	6	5	2.47	3	3.80	3.77	12	14
				D	6	6	2.66	3	4.09	4.06	12	14
				E	6	4	2.54	3	3.91	3.88	12	14
0454+844	...	0.112	B	...	6	4	0.14 ± 0.04	3	0.70 ± 0.20	0.69 ± 0.20	13	4
0458−020	...	2.286	Qc	...	6	2	0	1	0.00	0.00	7	14
0552+398	DA 193	2.365	Qp	...	6, 4	2	0.04 ± 0.02	1	2.67 ± 1.34	1.72 ± 0.86	14	
0615+820	...	0.71	Qc	...	6	2	0.05 ± 0.05	1	1.30 ± 1.30	1.12 ± 1.12	15	16
0710+439	...	0.518	Qp	A	6	3	0.003 ± 0.008	3	0.06 ± 0.16	0.05 ± 0.14	16	
0711+356	...	1.620	Qc	...	6	3	0	2	0.00	0.00	4	14, 17, 18
0716+714	...	...	B	...	6	2	0.09 ± 0.11	1	...	...	6	17, 19
0723+679	3C 179	0.846	Ql	...	3	7	0.19	3	5.72	4.75	17	14
0735+178	...	>0.424	B	B	6	4	0	1	0.00	0.00	18	14, 17, 20
				C0*	6	3	0.44 ± 0.03	1	>7.43 ± 0.51	>6.76 ± 0.46	18	21, 22
0833+654	3C 204	1.112	Ql	...	4	2	−0.02 ± 0.04	1	−0.75 ± 1.50	−0.59 ± 1.18	19	
0835+580	3C 205	1.534	Ql	...	4	2	−0.01 ± 0.09	1	−0.48 ± 4.33	−0.35 ± 3.17	19	
0836+710	...	2.172	Qc	B*	6	2	0.23 ± 0.05	1	14.43 ± 3.14	9.56 ± 2.08	20	23
				C	6	4	0	1	0.00	0.00	20	1, 14, 23
				D	6	4	0.14 ± 0.05	2	8.78 ± 3.14	5.82 ± 2.08	20	23
0839+616	...	0.862	Ql	...	4	2	0.0 ± 0.03	1	0.00 ± 0.92	0.00 ± 0.76	19	24
0850+581	...	1.322	Qc	...	6	3	0.12 ± 0.02	2	5.15 ± 0.86	3.91 ± 0.65	21	
0851+202	OJ 287	0.306	B	K1	6	3	0.20 ± 0.03	2	2.54 ± 0.38	2.37 ± 0.36	22	
				K2*	6	3	0.27 ± 0.03	2	3.43 ± 0.38	3.20 ± 0.36	22	
0906+430	3C 216	0.67	Qcl	A*	6	3	<0.013	1	<0.32	<0.28	23	25
				B	6	4	0.18 ± 0.03	2	4.48 ± 0.75	3.86 ± 0.64	23	26
0923+392	4C 39.25	0.698	Q	A*	4	8	0	3	0.00	0.00	24	14
				B	3	3	0.18 ± 0.01	3	4.63 ± 0.26	3.97 ± 0.22	25	27
				D	1, 0.7	2	<0.022	1	<0.57	<0.49	26	
1039+811	...	1.26	Qc	...	6	2	<0.07	1	<2.89	<2.22	1	1, 5
1040+123	3C 245	1.028	Qcl	A2	3	2	0.11 ± 0.05	1	3.87 ± 1.76	3.10 ± 1.41	27	
1101+384	Mrk 421	0.031	B	C1	6	3	1.33 ± 0.02	1	1.92 ± 0.03	1.91 ± 0.03	28	21
				C2*	6	3	0.94 ± 0.15	1	1.36 ± 0.22	1.35 ± 0.22	28	
1127−145	...	1.187	Qp	...	6	2	0 ± 0.02	2	0.00 ± 0.79	0.00 ± 0.61	7	
1137+660	3C 263	0.646	Ql	...	3	3	0.06 ± 0.02	2	1.45 ± 0.48	1.25 ± 0.42	29	28
1150+812	...	1.25	Qc	C2	6	3	0.11 ± 0.05	3	4.52 ± 2.05	3.48 ± 1.58	6	17
1156+295	...	0.729	Q	...	6	2	1.15	1	30.66	26.11	30	14, 29
1222+216	4C 21.35	0.435	Ql	B	6	2	0.09 ± 0.04	1	1.55 ± 0.69	1.41 ± 0.63	31	30

TABLE 1—*Continued*

IAU Name (1)	Common Name (2)	z (3)	Classification (4)	Component ID (5)	Observation Wavelength (cm) (6)	Number of Epochs (7)	Proper Motion μ (mas yr^{-1}) (8)	Reliability (9)	$\beta_{app}h$ $q_0 = 0.05$ (10)	$\beta_{app}h$ $q_0 = 0.5$ (11)	References (12)	Notes (13)
1226+023	3C 273	0.158	Qc	C2	13, 6	8	1.15 ± 0.15	2	7.99 ± 1.04	7.71 ± 1.01	32	
				C3	6, 3	10	0.79 ± 0.03	3	5.49 ± 0.21	5.30 ± 0.20	33	
				C4*	6, 3	6	0.99 ± 0.24	2	6.88 ± 1.67	6.64 ± 1.61	33, 34	
				C5	3	5	1.20 ± 0.03	2	8.34 ± 0.21	8.04 ± 0.20	34	
				C7	4, 3, 1	6	0.65 ± 0.09	2	4.52 ± 0.63	4.36 ± 0.60	35	31
				C7a	3	3	0.76 ± 0.05	3	5.28 ± 0.35	5.09 ± 0.34	34	31
				C8	4, 3, 1	6	0.92 ± 0.11	3	6.39 ± 0.76	6.17 ± 0.74	35	
				C9	0.7	2	0.82 ± 0.12	1	5.70 ± 0.83	5.50 ± 0.80	36	
1228+127	M87	0.0032	G	N2	18	3	1.1 ± 0.3	2	0.17 ± 0.05	0.17 ± 0.05	37	32
1253−055	3C 279	0.538	Qc	...	4	6	0.5 ± 0.1	1	10.35 ± 2.07	9.18 ± 1.84	38	33, 34
				C3*	6, 3, 1	12	0.12 ± 0.02	3	2.48 ± 0.41	2.20 ± 0.37	39	
1308+326	...	0.996	B	K1	6	2	0.13	1	4.46	3.60	40	35
				K2	6	2	0.75	1	25.73	20.77	40	35
				K3*	6	2	0.29	1	9.95	8.03	40	35
1322−427	Cen A	0.0008	G	...	4	2	4.0 ± 0.8	1	0.15 ± 0.03	0.15 ± 0.03	41	36, 37
1458+718	3C 309.1	0.905	Qc	*	6	3	0.25 ± 0.15	1	7.94 ± 4.77	6.53 ± 3.92	42	38
				B	6	3	0 ± 0.03	1	0.00 ± 0.95	0.00 ± 0.78	42	
1607+268	CTD 93	0.473	Qp	...	6	2	0 ± 0.025	1	0.00 ± 0.46	0.00 ± 0.42	43	
1618+177	3C 334	0.555	Ql	...	3	3	0.10 ± 0.03	2	2.13 ± 0.64	1.88 ± 0.56	44	
1637+826	NGC 6251	0.023	G	...	18	2	0.05 ± 0.07	2	0.05 ± 0.08	0.05 ± 0.08	45	39, 40
1641+399	3C 345	0.594	Qc	C2	13, 6, 3	13	0.47 ± 0.02	3	10.58 ± 0.45	9.26 ± 0.39	46	41
				C3*	13, 6, 3, 1	14	0.30 ± 0.01	3	6.75 ± 0.23	5.91 ± 0.20	46	41
				C4	3, 1	11	0.31 ± 0.01	3	6.98 ± 0.23	6.11 ± 0.20	46	41, 42
				C5	3, 1, 0.7	14	0.23 ± 0.03	3	5.18 ± 0.68	4.53 ± 0.59	47	43
1642+690	...	0.751	Qc	...	6	2	0.34 ± 0.04	2	9.29 ± 1.09	7.87 ± 0.93	48	17
1721+343	4C 34.47	0.206	Ql	B	6, 3	6	0.16 ± 0.05	2	1.42 ± 0.44	1.36 ± 0.42	49, 50	
				C*	6, 3	6	0.28 ± 0.03	2	2.49 ± 0.27	2.37 ± 0.25	49, 50	
1749+701	...	0.77	B	...	6	2	0.26 ± 0.03	1	7.25 ± 0.84	6.12 ± 0.71	1	17, 44, 45
1803+784	...	0.68	B	...	6, 4	7	0.004 ± 0.028	3	0.10 ± 0.70	0.09 ± 0.61	1	4, 17, 46
1823+568	...	0.664	B	K1	6	2	0.12	1	2.96	2.56	13	14
1828+487	3C 380	0.691	Qc	A*	6	2	0.38 ± 0.025	1	9.69 ± 0.64	8.32 ± 0.55	51	47, 48
				B	4	2	0.23 ± 0.04	1	5.87 ± 1.02	5.04 ± 0.88	51	1, 47
1830+285	4C 28.45	0.594	Ql	B*	6	3	0.13 ± 0.04	2	2.93 ± 0.90	2.56 ± 0.79	31	
				C	6	3	0.13 ± 0.04	1	2.93 ± 0.90	2.56 ± 0.79	31	
1901+319	3C 395	0.635	Qc	2*	6	4	0 ± 0.03	3	0.00 ± 0.71	0.00 ± 0.62	52	
				3	6	3	0.64 ± 0.10	1	15.22 ± 2.38	13.22 ± 2.07	53	27
1928+738	...	0.302	Qc	A1	1	3	0.32 ± 0.10	3	4.01 ± 1.25	3.75 ± 1.17	54	
				B	1	5	0.37 ± 0.05	2	4.64 ± 0.63	4.34 ± 0.59	54	
				C	1	6	0.34 ± 0.03	3	4.27 ± 0.38	3.98 ± 0.35	54	
				C2	6	3	0.51 ± 0.10	2	6.40 ± 1.25	5.98 ± 1.17	6	
				C3*	6	4	0.57 ± 0.05	3	7.15 ± 0.63	6.68 ± 0.59	6	
				C4	6	4	0.40 ± 0.05	3	5.02 ± 0.63	4.69 ± 0.59	6	
				C6	6	3	0.40 ± 0.10	1	5.02 ± 1.25	4.69 ± 1.17	6	
				C7	6	3	0.60 ± 0.10	2	7.53 ± 1.25	7.03 ± 1.17	6	
				C9	6	2	0.31 ± 0.55	1	3.89 ± 6.90	3.63 ± 6.44	6	
1934−638	...	0.183	Qp	B	13	2	0.01 ± 0.03	1	0.08 ± 0.24	0.08 ± 0.23	55	49
1951+498	...	0.466	Ql	...	3	2	0.07	1	1.28	1.16	56	14
2007+777	...	0.342	B	C2	6	4	0.18 ± 0.04	2	2.52 ± 0.56	2.33 ± 0.52	6	17
2021+614	...	0.227	Qp	...	6	2	0.022 ± 0.022	1	0.21 ± 0.21	0.20 ± 0.20	4	1
2200+420	BL Lac	0.069	B	S1	3	4	1.2 ± 0.1	1	3.79 ± 0.32	3.73 ± 0.31	57	
				S2	3	4	1.1 ± 0.1	1	3.47 ± 0.32	3.42 ± 0.31	57	
				S3*	3	4	1.1 ± 0.1	2	3.47 ± 0.32	3.42 ± 0.31	57	
				S5	3	2	1.0 ± 0.1	1	3.16 ± 0.32	3.11 ± 0.31	57	

TABLE 1

COMPILATION OF INTERNAL PROPER MOTIONS

IAU Name (1)	Common Name (2)	z (3)	Classification (4)	Component ID (5)	Observation Wavelength (cm) (6)	Number of Epochs (7)	Proper Motion μ (mas yr^{-1}) (8)	Reliability (9)	$\beta_{app} h$ $q_0 = 0.05$ (10)	$\beta_{app} h$ $q_0 = 0.5$ (11)	References (12)	Notes (13)
2223−052	3C 446	1.404	Qc	...	6	3	0 ± 0.06	1	0.00 ± 2.70	0.00 ± 2.02	7	
2230+114	CTA 102	1.037	Qp	...	6	2	0 ± 0.5	1	0.00 ± 17.72	0.00 ± 14.19	58	50
2251+158	3C 454.3	0.859	Qc	2*	3	8	0.045 ± 0.016	2	1.37 ± 0.49	1.14 ± 0.40	59	
				3	3	4	−0.046 ± 0.072	1	−1.40 ± 2.19	−1.16 ± 1.82	59	
				4	3	4	0.35 ± 0.06	1	10.66 ± 1.83	8.84 ± 1.52	59	
				5	3	3	0.21 ± 0.05	1	6.40 ± 1.52	5.31 ± 1.26	59	
2352+495	...	0.237	Qp	A	6	2	<0.03	2	<0.30	<0.29	16	5, 51
				B2*	6	3	<0.03	3	<0.30	<0.29	16	5, 25, 51

NOTES.—(1) μ calculated from β_{app} data in the reference. (2) Map by Cawthorne et al. 1993 agrees with same μ. (3) Measurement is consistent with earlier 6 cm map by Preuss 1983. (4) Redshift from C. Lawrence 1993, private communication. (5) Only an upper limit to μ is available. (6) Also called 0235+285. (7) Redshift from Richstone & Schmidt 1980. (8) Inner component. (9) Consistent data exist at other wavelengths. (10) Redshift from Burbidge & Strittmatter 1972. (11) Double model from data taken in 1973–1974. No optical identification. (12) Error from K. I. Kellermann 1993, private communication. (13) Redshift from Sargent 1977. (14) An error estimate is not available. (15) Most of the points are at 6 cm. (16) Motion also published as upper limit by Schalinski et al. 1992. (17) Strong intraday variability has been observed; see Quirrenbach et al. 1992. (18) Conway et al. 1990 say component is "static." Variable structure between two stationary components may have led to earlier report of $\mu = -0.13 \pm 0.02$ in Readhead, Pearson, & Unwin 1984. See also Cawthorne et al. 1993. (19) This object has no redshift. (20) Absorption redshift, lower limit to emission redshift. (21) Motion is an average of two values in the reference. (22) See also the single-epoch results at 1.3 cm by Bååth, Zhang, & Chu 1991. (23) Redshift from Stickel & Kühr 1993. (24) 0.0 is the fitted value for μ. (25) Upper limit is not directly stated by authors but can be inferred from their discussion. (26) Motion is weighted fit to four positions, but first position may be affected by blending; deceleration cannot be ruled out. (27) Possible deceleration in fourth epoch. 3C 395: See Simon et al. 1988a. 4C 39.25: See Marcaide et al. 1989. (28) Redshift from Phillips 1977. (29) Consistent data exist at 1.3 and 2.8 cm. (30) Redshift is average of values in Lynds 1967 and Burbidge & Kinman 1966. (31) Component 7a is considered part of component 7 at later epochs (Cohen et al. 1987; Zensus et al. 1990). (32) Redshift from an assumed distance of 16 Mpc, with $H_0 = 60$ km s^{-1} Mpc^{-1}. (33) Measurements from 1970 to 1972 with a two-element interferometer; amplitudes modeled with a double. (34) Redshift is average of values in Lynds, Stockton, & Livingston 1965 and Burbidge & Rosenberg 1965. (35) Gabuzda et al. 1993 suspect that this high-luminosity object might be a quasar rather than a BL Lac object. (36) Redshift from an assumed distance of 4 Mpc, with $H_0 = 60$ km s^{-1} Mpc^{-1}. (37) Internal proper motion error bar given in Meier et al. 1993 is a misprint (D. L. Meier 1993, private communication). (38) Internal proper motion error represents range of quoted values in northern jet. (39) Internal proper motion is our fit to positions at two epochs given by Jones 1986. (40) Redshift from Waggett, Warner, & Baldwin 1977. (41) Internal proper motion is weighted combination of values given by Biretta, Moore, & Cohen 1986. (42) Component appeared to accelerate in 1982. Values are for the post acceleration motion. (43) Possible acceleration. (44) Tentative redshift, based on one emission line (Stickel, Fried, & Kühr 1989). (45) Cawthorne et al. 1993 report $\mu \sim 0.15$ mas yr^{-1}. (46) Upper limit is at 3.6 cm; higher limit known at 6 cm. Evidence exists for structural variations close to core. (47) Earlier sequence suggested different motions (Wilkinson et al. 1990), which are in turn not supported by a map at intermediate epoch of Cawthorne et al. 1993. Motion and brightness changes may be hard to disentangle. (48) We adopted μ and error from Polatidis, Wilkinson, & Akujor 1993; neither their stated β_{app} nor its stated error are obtained for their stated cosmology. (49) Hybrid map compared to model from early data. Error determined by us from quoted position errors. (50) Bååth 1987 measured a higher velocity at 966 MHz. (51) Motion measured with respect to component B1.

REFERENCES.—(1) Schalinski et al. 1992; (2) Venturi et al. 1993a; (3) Wehrle, Cohen, & Unwin 1990; (4) Conway et al. 1990; (5) Vermeulen et al. 1993; (6) Witzel et al. 1988; (7) Vermeulen & Cohen 1994; (8) Marr, Backer, & Wright 1990; (9) Marscher & Broderick 1985; (10) Bååth et al. 1980; (11) Preuss et al. 1990; (12) Walker, Benson, & Unwin 1987; (13) Gabuzda et al. 1989a; (14) Charlot 1990; (15) Schalinski 1990; (16) Conway et al. 1992; (17) Porcas 1987; (18) Bååth & Zhang 1991; (19) Hough et al. 1993; (20) Krichbaum et al. 1990a; (21) Barthel et al. 1986; (22) Gabuzda, Wardle, & Roberts 1989b; (23) Venturi et al. 1993b; (24) Shaffer et al. 1987; (25) Schalinski et al. 1988; (26) Alberdi et al. 1993; (27) Hough & Readhead 1987; (28) Zhang & Bååth 1990; (29) Zensus, Hough, & Porcas 1987; (30) McHardy et al. 1993; (31) Hooimeyer et al. 1992c; (32) Zensus et al. 1988; (33) Unwin et al. 1985. (34) Cohen et al. 1987; (35) Zensus et al. 1990; (36) Krichbaum et al. 1990b; (37) Reid et al. 1989; (38) Cotton et al. 1979; (39) Unwin et al. 1989; (40) Gabuzda et al. 1993; (41) Meier et al. 1993; (42) Kus et al. 1990; (43) Porcas 1990; (44) Hough et al. 1992; (45) Jones 1986; (46) Biretta, Moore, & Cohen 1986; (47) Zensus 1991; (48) Pearson et al. 1986; (49) Hooimeyer et al. 1992a; (50) Barthel et al. 1989; (51) Polatidis, Wilkinson, & Akujor 1993; (52) Simon, Johnston, & Spencer 1988b; (53) Simon et al. 1988a; (54) Hummel et al. 1992; (55) Tzioumis et al. 1990; (56) Zensus & Porcas 1987; (57) Mutel et al. 1990; (58) Wehrle & Cohen 1989; (59) Pauliny-Toth et al. 1987.

motions, and of upper limits on such motion. In all cases, the original publications, referenced in column (12), have been consulted. When proper-motion measurements are available for different components within one source, these are listed separately. Column (5) gives the component labels, if any. In sources with multiple velocities, the "brightest" component selected for our statistical studies is indicated by an asterisk in column (5); this selection will be discussed in § 2.2. The wavelength of the observations, or in some cases the combination of wavelengths, is listed in column (6). Column (7) gives the number of epochs at which the component positions were measured. The internal proper motion (μ) measurements are listed in column (8). In five cases (indicated by a reference to note 1 in col. [13]), μ was not given in the publication but had to be recomputed from the published apparent transverse velocity ($\beta_{\rm app}$) and the stated values of H_0 and q_0.

Errors on μ are listed in column (8) whenever available. These data are rather inhomogeneous and were determined using rather different methods. While we have decided not to use weights in our further analysis, we have attempted to use uniform criteria to place the objects into low (1), medium (2), and high (3) reliability categories, as an aid for the reader in comparing the tabulated data. Measurements in our high-reliability category meet all of the following conditions: (*a*) observations with at least four stations if the components are well separated and of comparable magnitude, or at least six stations with long tracks, or at least 12 stations in snapshot mode; (*b*) good maps at three or more epochs; (*c*) publication with an appropriate discussion of the methods used to locate the centroids of the components and their errors, and a least-squares or other suitable discussion of the velocity; and (*d*) components separated by at least one beamwidth. Measurements at only two epochs are mostly in category 1, which is also assigned whenever there is possible ambiguity over the tracking of components, and for component separations between 0.5 and 1 beamwidth, unless conditions *a*, *b*, and *c* are satisfied.

From the internal proper motion (μ), the apparent transverse velocity ($\beta_{\rm app}$) can be computed in Friedmann cosmology, using (e.g., Pearson & Zensus 1987):

$$\beta_{\rm app} = \mu \frac{z}{H_0(1+z)} \left[\frac{1 + (1+2q_0 z)^{1/2} + z}{1 + (1+2q_0 z)^{1/2} + q_0 z} \right]. \quad (1)$$

Columns (10) and (11) of Table 1 give the apparent transverse velocities and their errors for two values of the deceleration parameter: $q_0 = 0.05$ and $q_0 = 0.5$. All values are expressed in terms of h, but see the notes (listed in col. [13]) for 1228+127 (M87) and 1322−472 (Cen A).

2.2. *Uniformity and Reliability of the Data*

The data collected in Table 1 represent the result of the world's effort to measure superluminal motions over a period of ~20 years. Although numerous groups and individuals have pursued this subject diligently, there are no complete results as yet on a homogeneously selected sample of sources sufficiently large for a rigorous statistical analysis. However, if the data from the different monitoring programs are taken together, there are now a few source categories (see § 2.3) with sufficiently many objects to warrant a statistical study in this paper.

The current data set is inhomogeneous because of the widely different VLBI arrays used, and because of differences in data acquisition and analysis procedures. The formal errors in column (8) of Table 1 carry varied meanings. In many cases the error on the internal proper motion was derived from the formal errors attached to the locations of the component centroids; in others it was based on the beam size or on shifts arising with different starting models. Although these will generally give a good measure of the stability of the map-making procedure, they may seriously underestimate the systematic errors, which could be caused, for example, by substantial differences in the *uv* coverage from epoch to epoch, by incautious use of self-calibration procedures, or by inappropriate model fitting.

In some cases, only upper limits to the internal proper motion are given in the literature. For our statistical analysis below we have treated these upper limits as 1 σ errors on $\mu = 0$. We urge observers always to publish internal proper motions with errors (measured in mas yr^{-1}), based on formal fits to a series of positions, even when there is no significant motion.

As they move, some of the superluminal features expand significantly; this may also lead to systematic errors in the internal proper motion measurement. In a few of the best-studied sources, it is known that components follow a curved trajectory and may not have a constant velocity (e.g., 1641+399 [3C 345]; Zensus et al. 1994); in sources which are less closely monitored, this could be another source of systematic errors. In this paper we will adopt a simple model in which all superluminal motions are linear; at present this is the only practical way to proceed. It should also be mentioned that some of the objects, indicated by note 17 to Table 1, have been observed to undergo significant intraday variability, which may affect the aperture synthesis images of the sources.

Further inhomogeneity arises because the source in Table 1 were not all observed at the same linear resolution and emitted frequency. In fact, these two requirements need conflicting shifts in observing frequency with redshift. Some of the internal proper motion measurements in Table 1 incorporate data observed at more than one wavelength. This carries the risk of systematic errors—for example, due to differences in optical depth. Measurements at different wavelengths were kept separate whenever the original publications allowed this. There is also evidence that different phenomena may occur at frequencies below 1 GHz, for example in 2230+114 (CTA 102; see Bååth 1987 and Wehrle & Cohen 1989).

Many VLBI observations were done at 6 cm; this wavelength has traditionally yielded good data sets from a large number of antennas. A consistent treatment from source to source is important in our statistical analysis below. Therefore, we have taken 6 cm measurements in preference to all others, whenever a source has multiple internal proper motion values. Also with the aim of maximizing consistency, the jet component which reached the highest observed brightness was selected, whenever more than one was monitored at 6 cm. We believe this selection mimics the observational selection in less well studied sources, where typically a superluminal motion would only be found for the brightest jet feature. It is difficult to assess what bias, if any, is incurred by selecting the brightest components; the issue is explored in § 5 for the core-selected quasars (Q*c*'s in Table 1) by comparing the $\beta_{\rm app}$ distribution of the brightest and the fastest components. There are 13 sources (8 Q*c*'s) in which the brightest component is not the fastest, and 9 objects (4 Q*c*'s) in which the brightest component also has the largest $\beta_{\rm app}$; the other 44 sources (13 Q*c*'s) have only one measurement.

Another inhomogeneity results from the differing selection

criteria in the lists of objects chosen for monitoring. Many of the sources in Table 1 are part of samples selected at high frequency (e.g., Pearson & Readhead 1988; Witzel et al. 1988), from which we have attempted to define a more homogeneous group of 25 core-selected quasars (§ 2.3). It is also likely that the internal proper motion values published to date are a biased subset from those samples. First, some sources have not shown recognizable features which could be tracked; it is unknown whether these objects are otherwise different. Furthermore, it is possible that very rapid motion has been missed in a few objects, if the components also fade or expand quickly, or if there is a rapid succession of components, which could introduce ambiguities. Such events are seen in 0430+052 (3C 120), although of course its high μ does not correspond to an unusually high β_{app}, since it is at low redshift. However, there is a clear cutoff in the number of sources at high internal proper motions, which does not correspond to any observational limit above which they could suddenly become much more difficult to measure, or at which stroboscopic ambiguities would suddenly set in. Hence we believe that intrinsically much faster sources can form at most a small fraction of the superluminal population, unless the higher velocities are confined to angular scales below 1 mas. Conversely, Table 1 is likely to be deficient in sources with a relatively slow motion. These have been neither easy nor attractive objects to monitor and analyze. It should also be kept in mind that a fixed detection limit in μ leads to a β_{app} detection limit which increases with redshift.

2.3. *Source Classification*

Most of our further analysis, in § 5, concerns core-selected quasars, and this group should be as homogeneous as possible. First, all sources except 0355+508 (NRAO 150) were classified as either galaxies (G; seven objects) or BL Lac objects (B; 11 objects) or quasars (Q; 47 objects). We then defined more complex subcategories: gigahertz-peaked spectrum (*p*), lobe-selected (*l*), and core-selected (*c*) for the quasars.

The galaxies form a somewhat varied group of objects which are otherwise hard to classify. Inclusion or exclusion of some of these in other classes does not critically affect the statistics, and we have decided to keep them as a separate category. Note that they are all at $z < 0.05$, while the lowest redshift quasar in Table 1 (1226+023, 3C 273) is at $z = 0.158$. Two galaxies are superluminal, and five are subluminal.

The BL Lac objects all appear in the list by Stickel et al. (1991), except for 1101+384 (Mrk 421), which has a flux density below 1 Jy but meets their other criteria. The group includes 0716+714, without redshift, and 0735+178, with only a lower limit to its redshift. Otherwise, they span the redshift range $z = 0.031$ to $z = 0.996$; they may not be a homogeneous set of objects (see also § 2.4).

Next, within the quasars, we believe the gigahertz-peaked spectrum (GPS) sources (Q*p*'s in Table 1) should not be analyzed together with core-jet quasars, which typically have a flat spectrum. All the nine sources we have classified as Q*p*'s appear in at least one of the two lists by Stanghellini et al. (1990) and Dallacasa & Stanghellini (1990). They typically have little or no extended (arcsecond-scale) radio structure, and a variety of compact morphologies. Many are so-called compact doubles, compact triples, or compact-symmetric sources (e.g., Readhead et al. 1993), in which there are well-separated components with similar spectra, in at least some cases with connecting fainter emission (e.g., Conway et al. 1992). Their polarization characteristics are also different from those of core-jet quasars (e.g., Pearson & Readhead 1988; O'Dea, Baum, & Stanghellini 1991). However, there are a few ambiguous cases. For example, 0153+744 and 2021+614 could be similar objects (see, e.g., Pearson & Readhead 1988 for descriptions), but on the basis of spectrum and morphology we have decided to classify only 2021+614 as a Q*p*, because in 0153+744 only one component has a flat spectrum such that it is more reminiscent of a core-jet source. The inclusion or removal of a few uncertain cases would not qualitatively alter any of our conclusions regarding the Q*c*'s in § 5.

The remaining quasars were considered for inclusion in the Q*c* and Q*l* classes, defined below. Note that these two classes, in contrast to all others, are not mutually exclusive: 0906+430 (3C 216) and 1040+123 (3C 245) are in both subcategories.

The Q*c* and Q*l* groups should both contain only classical core-jet quasars, with a well-identified core. In 0923+392 (4C 39.25), superluminal motion occurs between a pair of bright stationary components, neither of which may be the core. Therefore, we have not included this object in any quasar subcategory.

We also wish to remark separately on 1156+295. Its superluminal velocity ($26\ h^{-1}c$ if $q_0 = 0.5$; see McHardy et al. 1993), if real, is much larger than what has been found with confidence in any other source, as is borne out in Figure 1. The value is based on two epochs at 6 cm, and hinges on correctly isolating a discrete feature in an unfavorable position angle along the jet. If this source represented the extreme in a continuous distribution of properties (e.g., Lorentz factors) in core-selected quasars, then, based on the discussion of upper envelopes in §§ 3 and 5, it would be difficult to understand why, in its redshift bin, β_{app} in 1156+295 is $\sim$2.5 times higher than that of the next fastest objects, of which there are quite a few with similar velocities (see Figs 1 and 2). The optical properties also seem to set 1156+295 apart: it is one of the optically most violently variable objects in the sky (e.g., Wills et al. 1983; Glassgold et al. 1983); when its continuum luminosity is high, 1156+295 would be classified as a BL Lac object on the basis of its optical spectrum. Indeed, as far as we can ascertain, 1156+295 is one of the few objects monitored for superluminal motion with VLBI after its *optical* properties drew attention to it. Note that 1156+295 is near the flux density cutoff for the core-selected quasars (*c*-quasars) (see below). It is possible that it somewhat resembles sources like 2134+004, in which peculiar morphological changes may not directly reflect any true motion. It is clearly important to monitor such sources closely. Given the extent to which all its properties seem to set 1156+295 apart, we have decided not to include it in any quasar subcategory.

For our analysis, the *l*-quasars should be a sample with a random distribution of jet angles, and hence selected on a property which is independent of beamed emission, such as the lobe emission at low frequency. The designation "*l*-quasar" has been reserved from those sources which belong to the three samples selected by Barthel et al. (1984; see also Hooimeyer et al. 1992b), Hough & Readhead (1989), and Zensus & Porcas (1987) (see Porcas 1981 for definition). This yields a total of 13 *l*-quasars. These sources have been monitored specifically to test beaming models which predict that they should have slower motions than many of the well-studied *c*-quasars.

In contrast, for our analysis the group of *c*-quasars should approximate as closely as possible a complete flux-limited sample including only classical core-jet quasars, selected on

TABLE 2

CORE-JET QUASARS: ADDITIONAL DATA

IAU Name (1)	Type (2)	$S_{c,6}$ (Jy) (3)	log R^a (4)	Reference (5)
1226+023	Qc	39.0	0.9	1, 2
1253−055	Qc	14.5	1.1	1, 2
2251+158	Qc	9.69	1.3	1, 2
1828+487	Qc	6.59	0.7	1, 3
1641+399	Qc	5.52	1.5	1, 2
0106+013	Qc	3.47	0.9	1, 4
1928+738	Qc	3.21	1.3	1, 2
1458+718	Qc	2.68	0.20	1, 5
0836+710	Qc	2.55	1.4	1, 6
0333+321	Qc	2.46	1.6	1, 2
2223−052	Qc	2.31	−0.15	1, 7
0212+735	Qc	2.20	>3.4	1, 8
0458−020	Qc	1.60	1.1	1, 9
0153+744	Qc	1.51	>2.0	1, 6
0711+356	Qc	1.50	>2.1	1, 6
0016+731	Qc	>1.50	>0.7	1, 10
1901+319	Qc	1.48	0.5	1, 2
0234+285	Qc	1.44	2.1	1, 11
1642+690	Qc	1.26	0.7	1, 2
1150+812	Qc	1.14	1.2	1, 6
1039+811	Qc	1.12	1.5	1, 6
0850+581	Qc	1.09	0.27	1, 12
0906+430	Qcl	1.06	−0.01	1, 5
0615+820	Qc	>0.90	>0.8	1, 10
1040+123	Qcl	0.86	−0.00	1, 5
1721+343	Ql	0.47	−0.05	12, 13
1830+285	Ql	0.45	−0.28	1, 12
1222+216	Ql	0.42	−0.01	1, 12
0723+679	Ql	0.32	−0.68	1, 14
1618+177	Ql	0.14	−0.64	1, 5
1137+660	Ql	0.129	−1.00	1, 5
1951+498	Ql	0.091	−0.24	15, 16
0133+207	Ql	0.066	−1.30	1, 5
0839+616	Ql	0.034	−0.94	15, 16
0835+580	Ql	0.023	−1.74	1, 5
0833+654	Ql	0.023	−1.36	1, 5

[a] The R-values given have been standardized to an emitted wavelength of 6 cm; when insufficient spectral information was available, a difference of 0.7 between the spectral index of the core and the lobes was assumed.

REFERENCES.—(1) Véron-Cetty & Véron 1991; (2) Browne 1987; (3) van Breugel et al. 1992; (4) Kollgaard, Wardle, & Roberts 1990; (5) Hough & Readhead 1989; (6) Browne & Perley 1986; (7) Simon, Johnston, & Spencer 1985; (8) Antonucci et al. 1987; (9) Briggs et al. 1989; (10) Ulvestad et al. 1981; (11) Antonucci & Ulvestad 1985; (12) Hooimeyer et al. 1992b; (13) Kühr et al. 1981; (14) Akujor 1992; (15) Gregory & Condon 1991; (16) Owen & Puschell 1984; (17) Pedlar et al. 1990; (18) Meier et al. 1993; (19) Turland 1975; (20) Mutel 1990; (21) Preuss et al. 1990; (22) Baum et al. 1990; (23) Waggett, Warner, & Baldwin 1977; (24) Venturi et al. 1993a.

TABLE 3

OTHER SOURCES: ADDITIONAL DATA

IAU Name (1)	Type (2)	$S_{c,6}$ (Jy) (3)	log R^a (4)	Reference (5)
0316+413	G	16.6	0.9	1, 17
0355+508	...	>10.2	>1.0	10
0923+392	Q	7.32	1.3	1, 2
1127−145	Qp	7.23	1.7	1, 6
1934−638	Qp	6.01[b]	...	1
1322−427	G	5	−1.3	13, 18
0552+398	Qp	>4.93	>0.6	1, 10
0430+052	G	4.41	0.8	1, 2
1228+127	G	4.0	−1.23	1, 19
2230+114	Qp	3.54	1.3	1, 20
2200+420	B	2.95	2.3	1, 2
1803+784	B	2.61	1.9	1, 20
0851+202	B	2.61	>3.4	1, 20
2021+614	Qp	>2.08	>0.9	1, 10
0735+178	B	1.99	>3.2	1, 20
1823+568	B	1.66	2.3	1, 20
2352+495	Qp	>1.63	>0.9	13, 10
1308+326	B	1.6	1.6	11
0710+439	Qp	>1.51	>0.9	1, 10
1607+268	Qp	>1.51	>0.9	13, 10
0454+844	B	1.40	>3.6	1, 20
0415+379	G	1.37	−0.69	1, 21
0108+388	Qp	1.33	2.3	13, 22
2007+777	B	1.26	1.8	1, 20
1749+701	B	1.09	2.7	1, 20
1156+295	Q	0.81	0.83	1, 11
1637+826	G	0.8	0.6	1, 23
1101+384	B	0.61	0.8	1, 20
0055+301	G	0.59	−0.0	13, 24
0716+714	B	0.49	−0.14	1, 6

[a] The R-values given have been standardized to an emitted wavelength of 6 cm; when insufficient spectral information was available, a difference of 0.7 between the spectral index of the core and the lobes was assumed.

[b] The total flux density is shown, since R is not known; R is expected to be large for Qp objects.

REFERENCES.—See Table 2.

their flux density *in beamed core emission*. In order to approximate a complete flux-limited sample, we have looked at the a posteriori flux density distribution for the classical core-jet sources. Table 2 is sorted by the core flux density observed at 6 cm (col. [3]), and also lists the core-to-lobe flux density ratios R (col. [4]), which were needed for some sources to convert their published total flux density to the core flux density. Since most of the objects are variable, the flux densities are somewhat arbitrary; there may even be a bias toward higher than average values, since many are from flux-limited samples. Furthermore, some R-values are simply lower limits based on the amount of detected lobe emission (or the lack thereof). For completeness the same data are given in Table 3 for the rest of the sources.

Table 2 shows that, starting at the highest flux densities, there is an increase in the number of objects in logarithmic flux density intervals, down to ~1 Jy, followed by a sharp decrease in the number density. There is a particularly wide gap between 0.86 Jy (1040+123, 3C 245), and 0.47 Jy (1721+343, 4C 34.47). The pattern in Table 2 obviously reflects the selection criteria imposed on the target lists of many groups, most notably the sources studied by Pearson & Readhead (e.g., 1988) and by Witzel et al. (e.g., 1988). For the purpose of assembling a group of c-quasars which is as large as possible, but is still at least a fair approximation to a flux-limited sample, a core flux density limit at 0.86 Jy seems to be appropriate. We suspect that the resultant sample of c-quasars is still deficient at low flux densities, but given the relatively small number statistics of Table 2 we do not see a better, more objective flux density level for a cutoff than the wide gap between 0.47 and 0.86 Jy.

Note again that the resultant c-quasar sample of 25 sources contains the two l-quasars 0906+430 (3C 216), and 1040+123 (3C 245). This is quite acceptable, since, in a sample of randomly oriented jets (l-quasars), some will be pointed fairly close to the line of sight, so that their Doppler-boosted flux density brings them into core-selected samples (c-quasars). It would be desirable to have internal proper motion measurements for a complete sample selected with a given a priori flux density

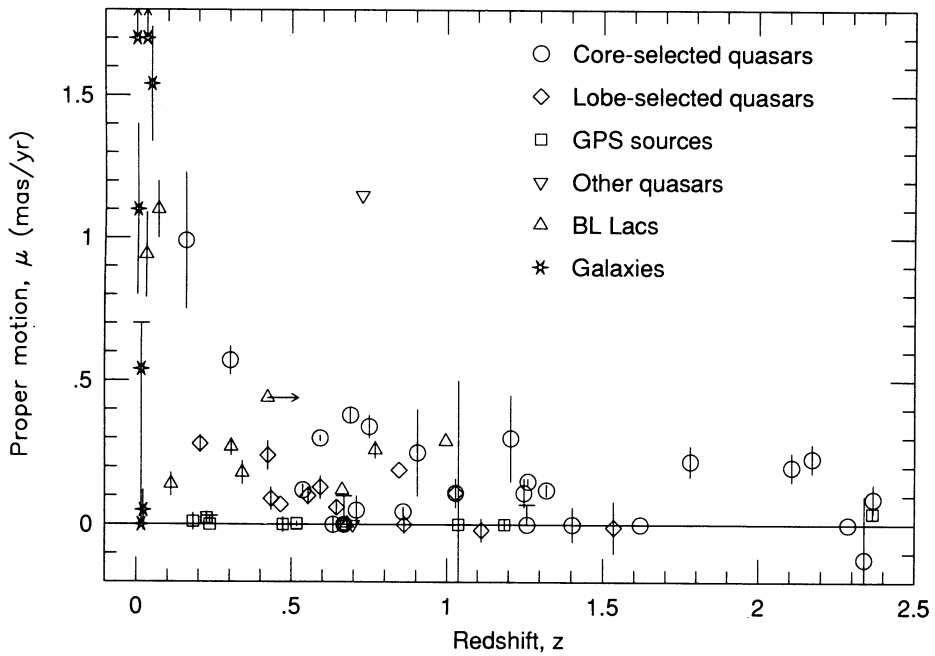

FIG. 1.—Internal proper motion–redshift (μ-z) diagram. For each source in Table 1, μ of the brightest component has been selected, with measurements at 6 cm taken in preference to all others. Error bars are shown where available. For objects with an upper limit, the source symbol is plotted at $\mu = 0$, with an error bar extending up to the limit. The two arrows pointing up indicate the galaxies 0430+052 (3C 120) and 1322−427 (Cen A), which fall outside the plotted region. The object 0735+278 is plotted at $z = 0.424$, which is a lower limit, as indicated. The outlying quasar is 1156+295.

limit; studies of such samples can now be undertaken with relative ease on the VLBA.

Note also that our definition of *l*-quasars does not explicitly involve a total or core flux density cutoff, or a limit on R. In practice, there is a good correspondence to a cutoff of $R \leq 1$, and to a core flux density ≤ 1 Jy (see Table 2 and Fig. 4, discussed below). The *l*-quasar category reaches to very low flux densities, and it is impossible to generate a flux-limited subsample.

2.4. *General Analysis*

Figure 1 displays the internal proper motions in Table 1 as a function of redshift; this has been termed the μ-z diagram. Whenever available, the formal errors have been plotted as well; upper limits have been treated as 1 σ errors on zero motions. The different source categories are shown with different symbols. As explained in § 2.2, only one measurement, for the brightest component (at 6 cm if available), is plotted per source, as indicated by asterisks in column (5) of Table 1. The internal proper motions decrease with redshift, as expected in Friedmann cosmology (e.g., Cohen et al. 1988).

Figure 2 shows β_{app}-z diagrams, with the apparent velocities from Table 1, columns (10) and (11), computed using Friedmann cosmology. It is clear that there is a rather well-defined upper envelope to the apparent velocities (with one outlier, 1156+295). As discussed in § 2.2, we believe that there are no selection biases or observational problems which could have conspired to make a significant population of faster sources go unnoticed. Note that the upper envelope is defined mostly by *c*-quasars; if $q_0 = 0.05$, the envelope seems to rise with redshift, whereas if $q_0 = 0.5$, it could well be flat (see § 5.6).

Figure 3*a* shows histograms of the β_{app} distributions in the different source classes if $q_0 = 0.5$. The hatched areas indicate sources with upper limits or (possibly negative) motions not significantly different from zero. The value of q_0 only makes a

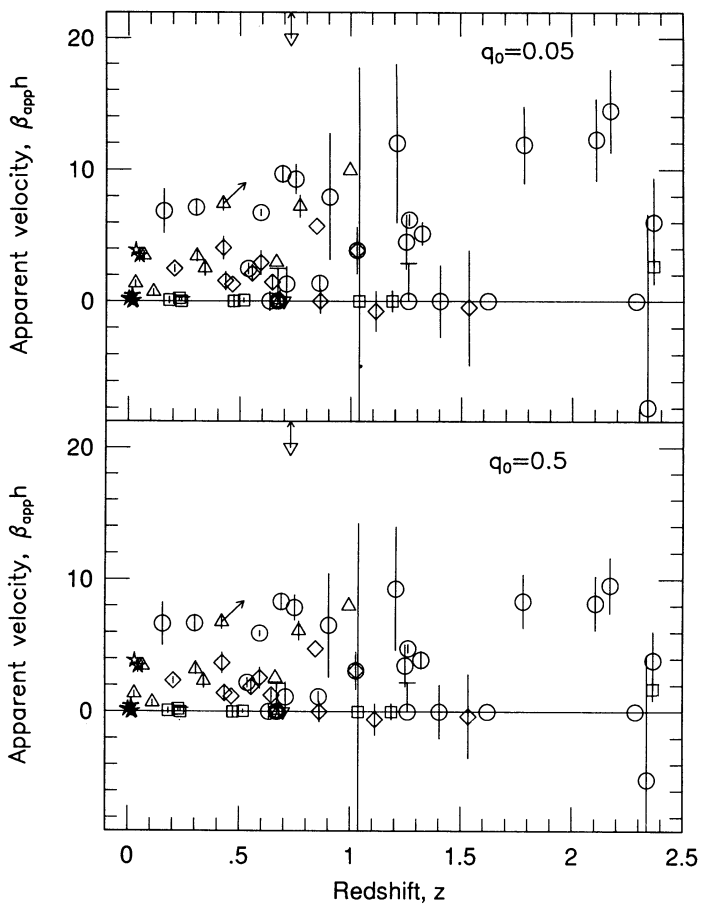

FIG. 2.—Apparent velocity–redshift (β_{app}-z) diagrams, assuming $q_0 = 0.05$ or $q_0 = 0.5$. Source category symbols and error bar treatment are as in Fig. 1. The quasar 1156+295 falls outside the plotted region.

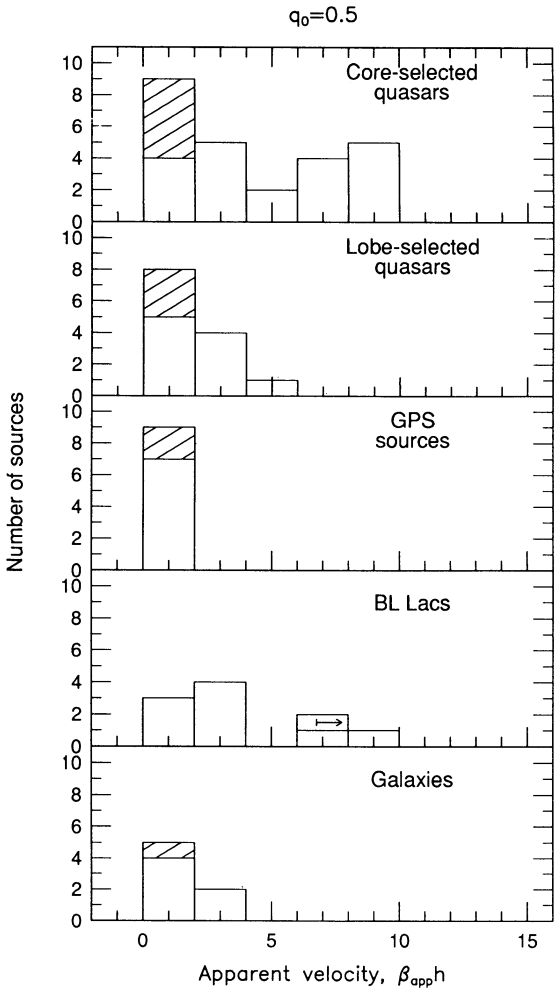

FIG. 3a

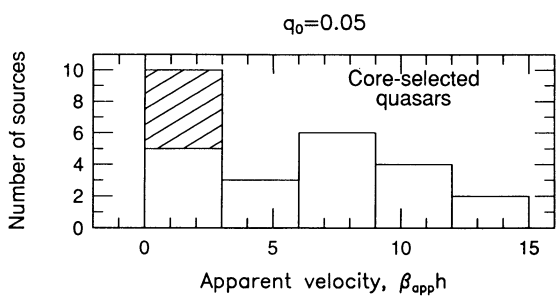

FIG. 3b

FIG. 3.—Histograms of the distribution of β_{app} values in various source categories. The hatched areas indicate sources with upper limits or (possibly negative) motions not significantly different from zero. In (*a*) $q_0 = 0.5$ is assumed, and in (*b*) the assumed value is $q_0 = 0.05$; this choice only makes a significant difference for the core-selected quasars.

significant difference for the *c*-quasars; Figure 3*b* shows the distribution for this class if $q_0 = 0.05$. With the possible exception of 0552+398 (DA 193), the nine Q*p*'s have no significant internal proper motion, supporting the validity of treating these sources as a separate class. This is the only group in which superluminal motions might be completely absent.

The data, depicted in Figures 1, 2, and 3, are consistent with unified schemes in which different object classes differ only in

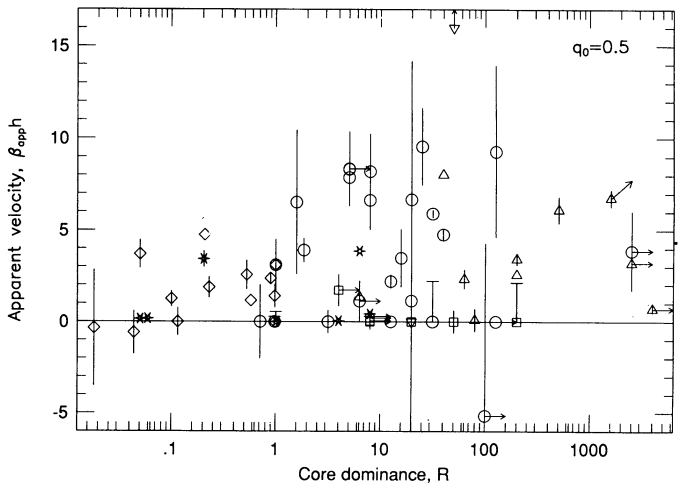

FIG. 4.—Values of β_{app} for $q_0 = 0.5$, as a function of the core dominance (R). Source category symbols and error bar treatment are as in Fig. 1; note that many R-values are lower limits. The quasar 1156+295 (log $R = 0.83$, $\beta_{app} = 26.11$) falls outside the plotted region.

the orientation of their jets with respect to the line of sight (see also, e.g., Ghisellini et al. 1993). However, given the heterogeneity of the data, especially in the smaller groups, they do not provide strong support, or firm constraints, for such unification models. It should be pointed out in particular that most of the galaxies have a rather lower luminosity than the quasars, and that the BL Lac objects span a wide range of luminosity. It is possible that lower luminosity objects intrinsically have lower β_{app} (e.g., Cohen 1989). Since the issue is not central to this paper, we have not attempted to pursue further refinements of the categories; we have striven to make the core-jet quasars the best homogeneous group, by not including in it any of the BL Lac objects and galaxies.

Figure 4 displays the apparent velocities for the different source classes against the core dominance R, for $q_0 = 0.5$ ($q_0 = 0.05$ gives qualitatively similar results). Note that many of our R-values are lower limits, as indicated. It appears that while β_{app} has a wide range at all values of R, there is an upper envelope, which rises with R up to $R \sim 100$; possibly, it then turns over. This relationship is exactly as predicted for sources at decreasing angles to the line of sight (e.g., Orr & Browne 1982; Brown 1987; Hough & Readhead 1987). The trend is most obvious in the *c*-quasars and *l*-quasars. Note that $R = 1$, which in some definitions is the boundary between lobe- and core-dominated objects, does not seem to have any special significance in this β_{app}-R diagram. It is also intriguing that the sequence seems to be completed, with slower velocities at the highest R, by BL Lac objects, as expected if these were very close to the line of sight. However, in view of the data inhomogeneity, and the many lower limits to R, the present data again do not provide strong support for any particular unification model.

3. BEAMING MODELS

Four simple beaming models are discussed in this section. They are introduced in § 3.1. In § 3.2 the assumptions which apply throughout our analysis are discussed. Section 3.3 demonstrates that, perhaps surprisingly, at small angles to the line of sight, Doppler favoritism is not very effective in selecting specific Lorentz factors from a distribution within a single

jet—a result needed for cases III and IV. The cumulative β_{app} distribution functions predicted in each of the four cases are then shown in §§ 3.4.1–3.4.4; case II, which is relevant for the analysis of core-selected quasar samples, is analyzed in the greatest depth. The four distributions are compared in § 3.5, and Figure 10 provides a synopsis of the main result. The effects of a possible maximum angle to the line of sight for quasar jets are discussed in § 3.6. In § 3.7 the differences between the β_{app} distributions for straight and bent jets are analyzed. Finally, it is shown in § 3.8 that the largest β_{app} encountered can often be a useful diagnostic even in a very small sample.

3.1. *Introduction*

We will discuss four basic models, labeled cases I–IV, by taking opposite extremes in two assumptions, as summarized in Table 4.

The first parameter is the range of Lorentz factors within a single jet. In cases I and II it is assumed that each jet is characterized by a single bulk Lorentz factor (which may, however, differ from source to source). Conversely, in cases III and IV, it is assumed that each jet contains a wide range of Lorentz factors and that the value actually observed is the one which is optimally Doppler-boosted (see § 3.3).

The second parameter is selection bias in orientation. In cases I and III a sample with jets pointing in random directions will be assumed; in § 4 we will compare those model predictions with the *l*-quasars defined in § 2. In cases II and IV, on the other hand, we will investigate the β_{app} distribution in a sample of sources selected by Doppler-boosted emission. Such sources, which we will compare in § 5 with the *c*-quasars, will have most of their jets pointed close to the line of sight.

The model variations focus mostly on kinematic aspects of superluminal motion, and they are surely oversimplifications of the physical reality in active galactic nuclei. Nevertheless, when compared with the observed apparent velocity distributions, they allow some interesting tentative inferences about the jets, which can serve as important guidelines in developing future, more sophisticated models. Furthermore, our analysis shows that some aspects of the predicted superluminal motion statistics are valid under a wide range of model assumptions, such that there are good prospects for using these statistics for cosmological goals.

3.2. *General Model Assumptions*

The following assumptions are made throughout:

1. The radio jets are narrow and straight between the location where they first become optically thin (the core) and the moving VLBI features. However, in § 3.7 the consequences of bending on parsec scales will be outlined. Furthermore, our analysis will also allow for a difference between the bulk flow velocity of the jets, denoted by β_b and $\gamma_b = (1 - \beta_b^2)^{-1/2}$ and responsible for Doppler boosting, and the velocity of a pattern in the jets, denoted by β_p and γ_p, and observable as superluminal motion. The consequences of having a very wide range of bulk velocities within each jet will also be explored (cases III and IV). With straight, narrow jets, the observed apparent velocity β_{app}, scaled by c, depends on the angle θ to the line of sight and on the pattern speed, according to

$$\beta_{app}(\theta, \gamma_p) = \frac{\beta_p \sin\theta}{1 - \beta_p \cos\theta} . \tag{2}$$

Therefore, we have $0 \le \beta_{app} \le \beta_p \gamma_p$; the maximum value occurs when $\cos\theta = \beta_p$.

2. The radio jets have a random intrinsic orientation with respect to our line of sight, but, whether or not sources are intrinsically two-sided, only approaching jets are observed. Thus,

$$p(\theta)d\theta = \sin\theta\, d\theta \quad \text{with} \quad 0 \le \theta \le \pi/2 . \tag{3}$$

This is a good assumption at small θ, owing to differential Doppler boosting, and thus far, even the observed lobe-selected quasars seem to have a single-sided core-jet morphology. Our analysis in §§ 4 and 5 assumes that the core can be correctly identified. Patterns moving in oppositely directed jets would yield $\beta_{app} \simeq 2$ (see also Pelletier & Roland 1990). Similarly, in cases II and IV, the contribution from a receding jet to the total observed flux density of a source will be ignored. This allows a more than adequate analytical expression of the dependence of the results on the free parameters n and q (defined in eqs. [5] and [6]). Exact solutions for two-sided jets can be obtained numerically after choosing values for n and a. In § 3.6 we will explore the consequences of having a cutoff pointing angle $\theta_{max} < 90°$.

3. The bulk Lorentz factors in the jets are determined for the entire source population by a single probability density function (pdf), $p(\gamma_b)$, with minimum and maximum possible values $\gamma_{b,min}$ and $\gamma_{b,max}$. In addition, there could be a separate pattern Lorentz factor γ_p. To obtain a global impression of its effects, it is useful to assume that γ_p is related to γ_b by a constant factor r, such that

$$r \equiv \frac{\gamma_p}{\gamma_b} , \quad \beta_p = \left(1 - \frac{1 - \beta_b^2}{r^2}\right)^{1/2} ,$$

and

$$\beta_b = [1 - r^2(1 - \beta_p^2)]^{1/2} . \tag{4}$$

In the simplest case, $r = 1$, there are no separate pattern velocities. It is not plausible that a fixed ratio r would hold over a very wide range of Lorentz factors; where such a wide range of values is assumed (cases III and IV), we will simply adopt $r = 1$.

No further assumptions are needed for case I. For the other cases, the following assumptions are also needed:

4. The standard Doppler boosting formula applies:

$$S_{obs} = S\left[\frac{1}{\gamma_b(1 - \beta_b \cos\theta)}\right]^n \equiv S\delta^n(\theta, \gamma_b) \tag{5a}$$

and

$$S_{obs} \equiv S_t\left(\frac{1}{1 - \beta_b \cos\theta}\right)^n . \tag{5b}$$

TABLE 4

OVERVIEW OF THE FOUR MODEL CASES

Case	Different γ_b in a Single Jet	Source Selection through Doppler Beaming
I	No	No
II	No	Yes
III	Yes	No
IV	Yes	Yes

Here S is the flux density which would be observed in a reference frame moving with the jet material, and S_t is the flux density which would be observed from a single jet if it were in the plane of the sky. For an optically thin sphere with spectral index α ($S \propto \nu^{\alpha}$), one should take $n = 3 - \alpha$; for a "string of bullets," or a continuous jet, $n = 2 - \alpha$ is appropriate (e.g., Scheuer & Readhead 1979). At the core the spectral index is usually quite flat, and we believe that $n = 1.8$ to $n = 2.3$ is a plausible range for our models; of course, more complicated scenarios are possible, which could give rise to different exponents (e.g., Lind & Blandford 1985). After discussing the dependence of our results on the value of n in §§ 3.4.2 and 3.4.4, we will adopt $n = 2$.

5. In an individual source there is no relationship between γ_b and/or γ_p and the emissivity (i.e., S). It is not clear whether this assumption is valid. We believe that there are arguments both for a positive and for a negative correlation, and that it is therefore reasonable in the first instance to explore models which assume that they are unrelated. For cases III and IV, which assume a wide range of Lorentz factors within each source, all portions will be taken to be equally emissive (see § 3.3).

For cases II and IV, the predictions applying to samples with a biased jet orientation distribution due to Doppler boosting, the following additional assumption will be made:

6. The differential source counts *when Doppler beaming is removed*, i.e., for S as used in equation (5), obey a single power law over a sufficient range in flux density $S_{\min}$ to $S_{\max}$. Thus,

$$dN(S) = KS^{-(q-+1)}dS \quad \text{with} \quad q \geq 1 , \tag{6a}$$

from which

$$p(S)dS = \frac{S^{-(q+1)}}{q(S_{\min}^{-q} - S_{\max}^{-q})}\, dS . \tag{6b}$$

The physical reality is undoubtedly more complicated. However, for the rather bright c-quasar sample under consideration in this paper ($S_{\text{obs}} > 0.86$ Jy), as well as for those which we can hope to investigate in the near future, a power-law approximation seems justified. The observed differential counts at 6 cm (which include beamed objects) seem to have $q \approx 1.5$; the range does not exceed 1.25–1.75 (e.g., Kapahi 1987). Since, as shown by Urry & Shafer (1984) and Urry & Padovani (1991), the luminosity functions before and after beaming have the sample slope at high luminosity, we do not believe Doppler beaming has had a large effect on the differential source count index. Note that in a homogeneous Euclidean universe $q = 1.5$, regardless of Doppler beaming, because the differential counts are then independent of the luminosity function. We will discuss the effect of modest changes in the power-law index q in §§ 3.4.2 and 3.4.4, and then adopt $q = 1.5$ as a representative value.

3.3. *Selection of Lorentz Factors by Doppler Beaming*

It is plausible that the mechanisms responsible for jet acceleration and collimation could lead to a range of velocities within a jet; this is our motivation for studying cases III and IV. We will take the jets to be intrinsically equally emissive for all $1 \leq \gamma_b \leq \gamma_{b,\max}$ (assumption 5). However, different values of γ_b lead to different Doppler boosting factors (δ), and this may limit the observable range of Lorentz factors. Figure 5 shows

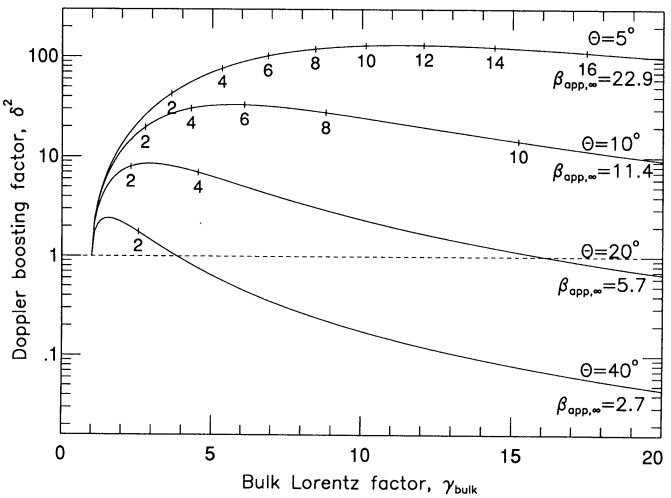

FIG. 5.—Doppler-boosting factor for continuous jets (δ^2), as a function of the Lorentz factor (γ_b), for jets at angles (θ) of 5°, 10°, 20°, and 40° to the line of sight. Tick marks also show the β_{app} values as a function of γ_b, and we note the maximum possible β_{app} at each θ, which occurs for $\gamma_b = \infty$. At small θ there is a wide range of γ_b which produces nearly the maximum Doppler boosting; it corresponds to a large range in β_{app}.

δ^2 ($S_{\text{obs}} \propto \delta^2$, assumption 4) as a function of γ_b for jets at different angles to the line of sight. There is an optimum Lorentz factor for each jet angle: a lower γ_b does not produce as much boosting, and for higher γ_b a larger fraction of the emission is beamed along the jet axis rather than toward the line of sight. The dependence on θ of the optimum γ_b for Doppler beaming can be found from equation (5) by setting $d\delta/d\beta_b = 0$; this yields

$$\beta_b = \cos\theta \quad \text{and} \quad \gamma_b = \frac{1}{\sin\theta} . \tag{7}$$

Note that while we use equation (7) here to find the optimum γ_b for Doppler boosting at a given angle to the line of sight, the same equation, in reverse, yields the θ with the fastest superluminal motion for given γ_b.

As can be seen in Figure 5, Doppler boosting is a strong function of γ_b at large θ. At small θ, however, the curves are fairly flat over a substantial range of γ_b values, which all yield almost the maximum Doppler boosting. Therefore, at small angles Doppler favoritism is not a good discriminant among Lorentz factors. Since a wide range of Lorentz factors corresponds to a wide range of β_{app}, as indicated by the labeled tick marks in Figure 5, Doppler boosting will not preferentially select a narrow range of β_{app} in jets at small θ. To first order, a wide range of β_{app} does not seem to be observed in many sources; instead, it is common to observe fairly well-defined features moving as a single entity. This suggests that individual radio jet features do not contain a wide range of γ_b, but it will be interesting to see whether the observation remains true as VLBI images reach progressively higher dynamic ranges at progressively higher resolution. Here we will study how β_{app} distributions in samples of objects at large or small θ vary depending on whether the observed β_{app} is selected from a wide range within each jet (cases III and IV), or not. Adopting equal pattern and bulk velocities ($r = 1$, assumption 3), the apparent velocity of the brightest feature can be found for a given θ by substituting equation (7) in equation (2), and taking account of

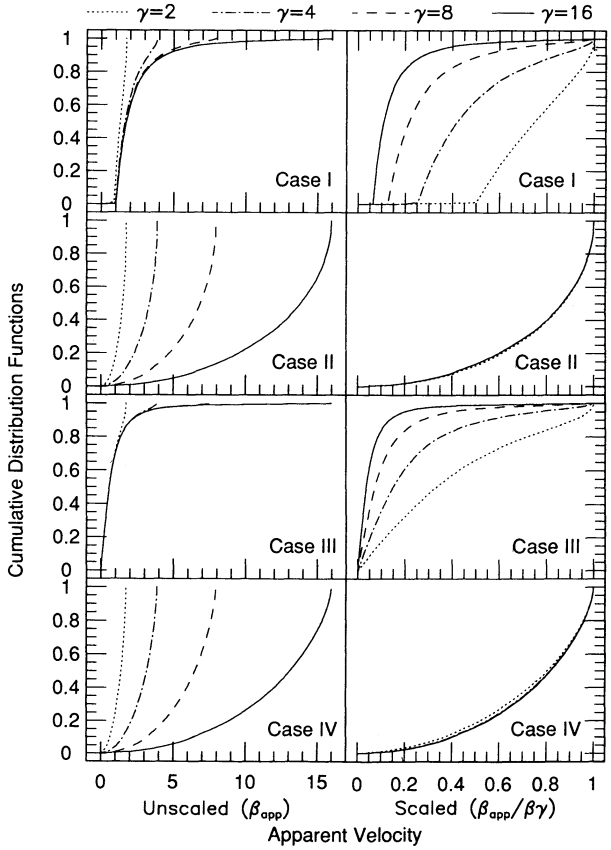

FIG. 6.—Predicted cumulative β_{app} distribution for $\gamma_p = \gamma_b = 2$, 4, 8, and 16, in the four model cases discussed in § 3. We use both unscaled (β_{app}) and scaled ($\beta_{app}/\beta\gamma$) apparent velocity axes, to illustrate that randomly oriented samples (cases I and III) always have a preponderance of low absolute β_{app} values, while in core-selected samples (cases II and IV) the relative β_{app} distribution is almost independent of γ.

the fact that there is an upper limit $\gamma_{b,max}$:

$$\beta_{app}(\theta) = \begin{cases} \dfrac{\beta_{p,max} \sin\theta}{1 - \beta_{p,max}\cos\theta}, & \sin\theta \le \dfrac{1}{\gamma_{b,max}}, \\ \dfrac{1}{\tan\theta}, & \sin\theta \ge \dfrac{1}{\gamma_{b,max}}. \end{cases} \quad (8)$$

3.4. *Apparent Velocity Distribution Functions*

In order to avoid binning, it is attractive to use predicted cumulative distribution functions (cdf's) for comparisons with the observed β_{app} data. Their mathematical derivation is given in the Appendix. Here we present the results, and discuss the sensitivity to some of the model parameters. The predictions for the four basic models are shown in Figure 6.

3.4.1. *Case I: Single Lorentz Factor; Random Jet Angles*

Since there is no selection on Doppler-boosted emission, the β_{app} distribution in case I depends only on the pattern Lorentz factors. An impression of likely cdf's can easily be obtained by first assuming that all sources have the same fixed pattern Lorentz factor, $\gamma_{p,f}$, and then plotting the predictions for different values of this parameter; this is done in Figure 6*a*, based on equation (A6). Almost independent of the value of $\gamma_{p,f}$, most of the apparent velocities lie in the range 1–2 (actually starting at $\beta_{app} \ge \beta_{p,f}$). These are mostly found in jets near the plane of the sky, where there is much solid angle. There are only a very few apparent velocities in the range $\beta_{app} < \beta_{p,f}$, which occur for jets in a narrow cone around the line of sight. Thus, there is a break in the cdf at $\beta_{p,f}$; the differential distribution (eq. [A7]) is not continuous there. Note that there is also a slight upturn in the cdf near the maximum allowed apparent velocity ($\beta_{app} = \beta_{p,f}\gamma_{p,f}$); this reflects the fact that $\beta_{app}(\theta)$ (eq. [2]) is flat at the maximum β_{app}.

3.4.2. *Case II: Single Lorentz Factor; Doppler Boosting Orientation Bias*

It is illustrative to assume first that the bulk Lorentz factor is the same in all sources ($\gamma_{b,f}$); we call this case IIa. In our comparison with the data in § 5, we will also use case IIb, in which there is a distribution $p(\gamma_b)$ over the sources.

Sources selected on Doppler-boosted emission will predominantly have their jets oriented at small angles to the line of sight. This is illustrated in Figure 7, which shows $p(\theta)$ from equation (A15), for $a = 2$ (a is discussed below). As shown in the Appendix, this function, as well as $p(\beta_{app})$, which follows from it, is independent of flux density. Note that $\theta \approx 1/(2\gamma_{b,f})$ is the most likely angle, whereas $\theta = 1/\gamma_{b,f}$ maximizes β_{app} if there are no separate pattern velocities ($r = 1$).

Figure 6*b* shows the cdf in equation (A17), for different $\gamma_{p,f} = \gamma_{b,f}$, with $a = 2$. Many large values of β_{app}, close to the maximum possible, are indeed predicted. Note that in equation (A17) β_{app} appears only in scaled form ($\beta_{app}/\beta_{p,f}\gamma_{p,f}$ within D_f), such that the shape of the scaled cdf curve (right-hand side of Fig. 6*b*) is virtually independent of $\gamma_{p,f}$. We have verified that even in more complicated models (e.g., $r \ne 1$, or case IIb), the absolute value of $\gamma_{b,f}$ is unimportant, as long as it is relativistic ($\gamma_{b,f} \ge 2$); in our further numerical simulations, we have used $\gamma_{b,f} = 8$.

In Figure 8 the scaled cdf from equation (A16) is shown for different values of r, again with $a = 2$. Numerical tests show that the steepest cdf, with the largest fraction of high velocities, has $r \approx 1.5$. Qualitatively, this corresponds to the fact that for $r \ll 1.5$, Doppler boosting is more extreme than the time compression effects which lead to superluminal motion, and thus the jet angles predominantly selected are rather smaller than those for which the largest values of β_{app} occur (see also Fig. 7

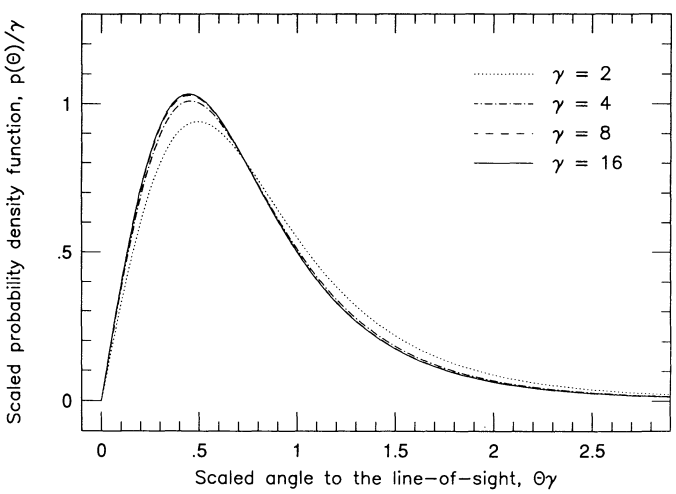

FIG. 7.—Probability density function $p(\theta)$ for $\gamma_p = \gamma_b = 2$, 4, 8, and 16 in case IIa (a core-selected sample). The axes are scaled to emphasize that the most likely angles to the line of sight are inside those of the largest β_{app}, $\theta = 1/\gamma$.

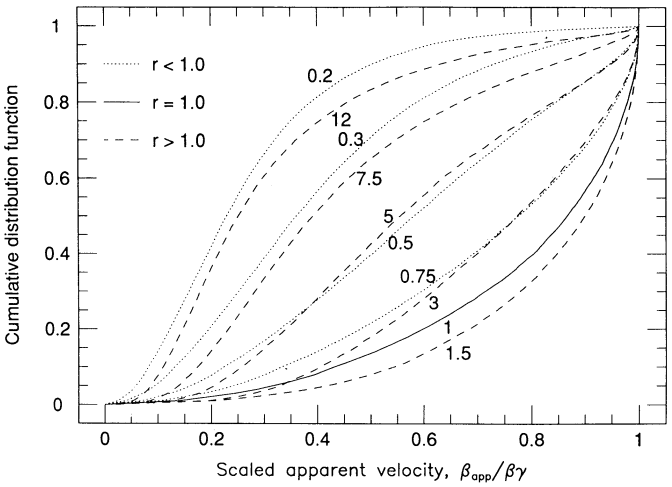

FIG. 8.—Predicted cumulative β_{app} distribution for different values of $r \equiv \gamma_p/\gamma_b$ in case IIa (a core-selected sample). The largest fraction of high β_{app} occurs for $r \simeq 1.5$; lower r (*dotted curves*) and higher r (*dashed curves*) can produce very similar β_{app} distributions, with an increasing fraction of low β_{app} for more and more extreme r.

and eq. [A15], in which $r = 1$). Conversely, for $r \gg 1.5$, the largest values of β_{app} occur at small angles to the line of sight, but these are not favored strongly enough by Doppler boosting. Thus, more slow velocities are seen both for very small and for very large r. Note that curves for high and low r sometimes cross. This is due to differences in the fraction of sources at very small angles, where β_{app} changes rapidly from its maximum value to zero.

Case II depends on the Doppler-boosting index and the source count index through the parameter $a \equiv nq - 1$. A numerical analysis shows that, for $r = 1$ (eq. [A17]), the most extreme cdf, rising steeply near the maximum possible β_{app}, occurs when $a = \sqrt{2}$: the cdf flattens for both smaller and larger a. Figure 9 shows how the cdf varies with a and r. The extreme values in $1.25 \leq a \leq 3.0$ correspond to simultaneously taking both of the lower limits or both of the upper limits in $1.8 \leq n \leq 2.3$ and $1.25 \leq q \leq 1.75$ (those ranges are discussed in § 3.2). The results are least sensitive to a at $r \approx 1$, but even for more extreme r, the range of cdf curves possible for different a is sufficiently narrow that useful estimates of likely values of r are feasible from an observed β_{app} distribution. Note that the upper and lower a curves are interchanged between low and high r. The dependence of the cdf on a can be understood qualitatively by viewing it as a result of different degrees of Doppler boosting (the parameter n). Too little Doppler boosting (low n) will not strongly select jets in which large apparent velocities can be observed. Too much Doppler boosting will preferentially select jets as such small angles that the apparent velocities are small again. Henceforth, we will use $a = 2$.

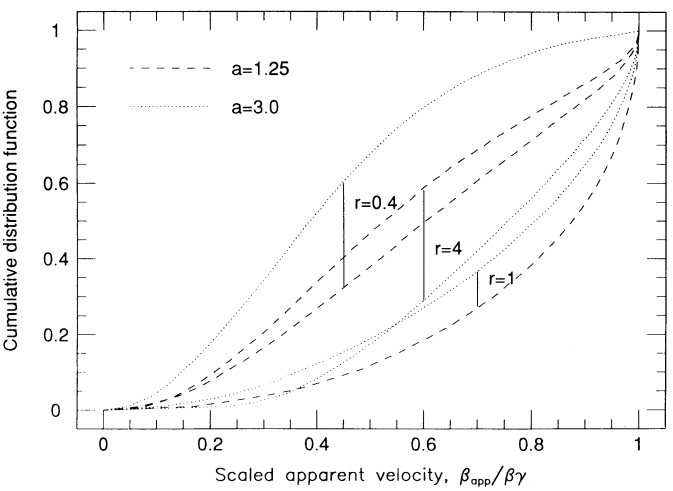

FIG. 9.—The sensitivity of the predicted cumulative β_{app} distribution in case IIa (a core-selected sample) to the parameter $a \equiv nq - 1$ is less at $r \simeq 1$ than at small or large r. The extremes $a = 1.25$ and $a = 3.0$ are discussed in the text; we have adopted $a = 2$ throughout this paper.

3.4.3. *Case III: Large Range of Lorentz Factors; Random Jet Angles*

In this case, Doppler favoritism is assumed to determine the β_{app} observed for a source at given θ, but it does not affect source selection, and the distribution of angles is unbiased (eq. [3]). The results therefore do not depend on bulk Lorentz factors but only on the range of pattern Lorentz factors $\gamma_{p,min}$–$\gamma_{p,max}$; $\gamma_{p,min}$ was taken to the subrelativistic in all cases. The predicted cdf, from equation (A18), is shown in Figure 6*c*, for different $\gamma_{p,max}$, which we here assume to be the same in every source. Most β_{app} are in the range 0–1, because in the large group of sources near the plane of the sky, low γ_p are favored by Doppler selection; in fact, for jets in the plane of the sky, stationary matter would have the highest brightness, all other things being equal (eq. [8]).

3.4.4. *Case IV: Large Range of Lorentz Factors; Doppler Boosting Orientation Bias*

Assuming the same $\gamma_{b,max} = \gamma_{p,max}$ in all sources, as in case III, the predicted β_{app} cdf is given by equation (A22) and is depicted in Figure 6*d* for different $\gamma_{p,max}$. We have again adopted $a = 2$, and we verified that the sensitivity to this parameter is similar to that in case II (see Fig. 9). Clearly, the apparent velocities in case IV are strongly dominated by the value of $\gamma_{p,max}$. This is due to the fact that most of the sources selected on Doppler-beamed emission will have a small angle to the line of sight—in which case large Lorentz factors *are* the most favorable ones (see Fig. 5).

3.5. *Comparison of the Four Model Cases*

In Figure 10 we compare the four model cases for $\gamma_b = \gamma_p = 8$; for cases I and II this is the single Lorentz factor, while for cases III and IV it is the maximum Lorentz factor in the range. These scaled distributions are not qualitatively altered as long as the Lorentz factor is greater than 2 (see Fig. 6).

First, we note that the randomly oriented samples (cases I and III) have quite the opposite distribution to the samples selected on beamed emission (cases II and IV): fast velocities are rare in the random samples, while they predominate in the others. It is interesting to note that the distribution for randomly oriented samples is only skewed in favor of low velocities in the relativistic case, when superluminal motion can occur in a small fraction of sources close to the line of sight. In the nonrelativistic limit, projection can yield only slower β_{app} at smaller angles to the line of sight. Hence, the solid angle available would yield a preponderance of the faster objects. It is easy to derive the cdf for randomly oriented nonrelativistic jets:

$$P(\beta'_{app} \leq \beta_{app}) = 1 - \left[1 - \left(\frac{\beta_{app}}{\beta_p}\right)^2\right]^{1/2}. \quad (9)$$

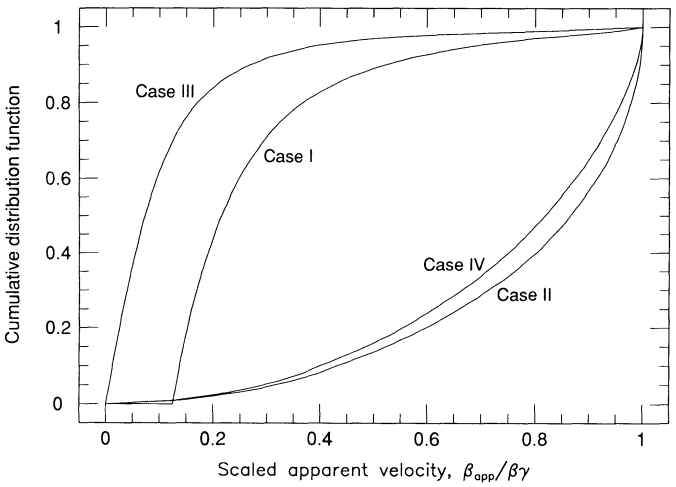

FIG. 10.—Comparison of the predicted cumulative β_{app} distribution in the four model cases (§ 3)

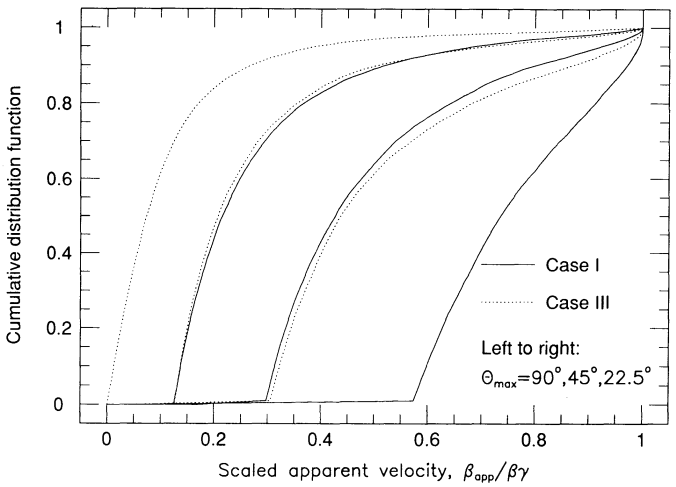

FIG. 11.—Predicted cumulative β_{app} distribution for maximum angles to the line of sight $\theta_{max} = 90°$, 45°, and 22°.5, in randomly oriented samples. There are ambiguities between case I (*solid lines*; single γ per jet) and case III (*dotted lines*; broad internal spread of γ per jet).

It can be verified with the definition of D_f (eq. [A1c]) that if $a = 2$, then in scaled form equation (A17) for case IIa (biased relativistic jet orientations) reduces to the nonrelativistic random orientation case (eq. [9]). We do not know whether this has any particular physical significance.

Comparing the two distributions for samples selected on Doppler-boosted emission, we note that the cdf predicted when selecting the optimum Lorentz factor from a wide range (case IV), is in fact only slightly less extreme than under the assumption that in all sources the same Lorentz factor is observed (case IIa). To get roughly matching distributions in unscaled velocities, $\gamma_{b,f}$, the single Lorentz factor of case IIa, must correspond to $\gamma_{b,max}$, the high end of the range of Lorentz factors allowed in case IV. As noted in § 3.4.4, this is because at small angles to the line of sight large Lorentz factors are the most favorable for Doppler favoritism. Lower Lorentz factors, though more favorable at larger angles to the line of sight, never yield as much Doppler boosting (see Fig. 5), and so only a few objects at large angles are ever selected, either in case II or in case IV. Given that there is little distinction between the predicted distributions for cases II and IV, and since at small angles to the line of sight it appears that Doppler favoritism is not a good way to select a specific Lorentz factor from a wide range (see § 3.3), we will drop case IV and compare only the simpler case II to the data on *c*-quasars in § 5.

For randomly oriented samples, allowing a wide range of Lorentz factors (case III) does lead to a pronounced difference from the single-γ case I: most of the velocities in case III are subluminal, rather than being in the range 1–2. There is no break in the cdf for case III. Otherwise, the shapes of the curves are similar. It is not clear whether it is realistic to allow the distribution of Lorentz factors within each jet (case III) to include the rather low values which give rise to the many subluminal velocities, but it should be noted that for jets at large angles to the line of sight, low Lorentz factors are strongly favored by Doppler boosting selection (see Fig. 5). If there were a lower cutoff to the range of Lorentz factors, then the β_{app} distribution would shift up accordingly, with a preponderance of cases then occurring at velocities just above $\beta_{app} = \beta_p$ of the lowest Lorentz factor. The distribution would of course resemble case I more and more for successively higher cutoffs and correspondingly narrower Lorentz factor ranges.

3.6. *The Effects of a Limit in Angle to the Line of Sight*

There are quasar and radio galaxy unification hypotheses in which these classes only appear to be different because their jets are oriented differently. Here we investigate the effects on the predicted β_{app} distribution of having a maximum angle to the line of sight (θ_{max}) in quasars.

A sample selected on beamed emission (case II) will predominantly have jets oriented at small angles (provided that $\gamma_b \geq 2$). Hence, for quasar samples selected on beamed emission, even a drastic restriction in angle to the line of sight (e.g., $\theta_{max} = 45°$) has only a minor effect on the predicted distribution of β_{app}.

In contrast, introducing a θ_{max} does have significant effects for intrinsically randomly oriented samples (cases I and III), as can be seen in Figure 11. The lowest velocities are almost all progressively eliminated for more and more severe θ_{max}, since low velocities mostly arise in the objects closest to the plane of the sky, which would normally dominate the sample. The resultant distributions still have a predominance of velocities immediately above the cutoff. The effect is similar for both high and low values of the (maximum) pattern Lorentz factor, as can be seen from Figure 6. Figure 11 shows an intriguing way to obtain very similar β_{app} distributions under cases I and III: the curve for any θ_{max} under case I is matched almost exactly by the curve with $\theta_{max}/2$ under case III. This degeneracy may prove to be a serious handicap for the interpretation of the velocity statistics obtained for samples of intrinsically randomly oriented quasars (e.g., the *l*-quasars), as will be discussed more fully in § 4.

3.7. *Bent Jets*

If jets bend on parsec scales, between the VLBI core, which we assume governs source selection, and the moving knots, then the predicted β_{app} cdf will be affected. For case I, the modifications will be minor, since most jets have a large angle to the line of sight, such that even a substantial bend will not change β_{app} much (see eq. [2]). However, in jets oriented close to the line of sight, which dominate in case II, β_{app} changes rapidly with bending. We have probed this in Monte Carlo simulations. The effects are easiest to recognize in the simplest

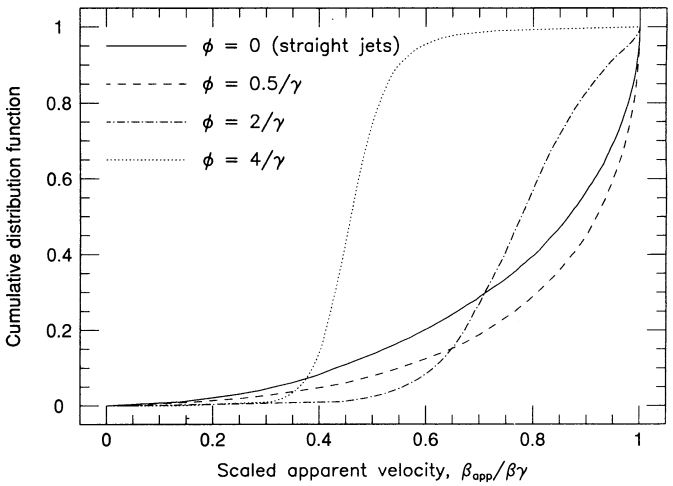

FIG. 12.—Predicted cumulative β_{app} distribution in case IIa ($r = 1$) for jets bent through an increasing angle ϕ (in a random azimuth). The fraction of high β_{app} increases while $\phi < 1/\gamma$, and then decreases.

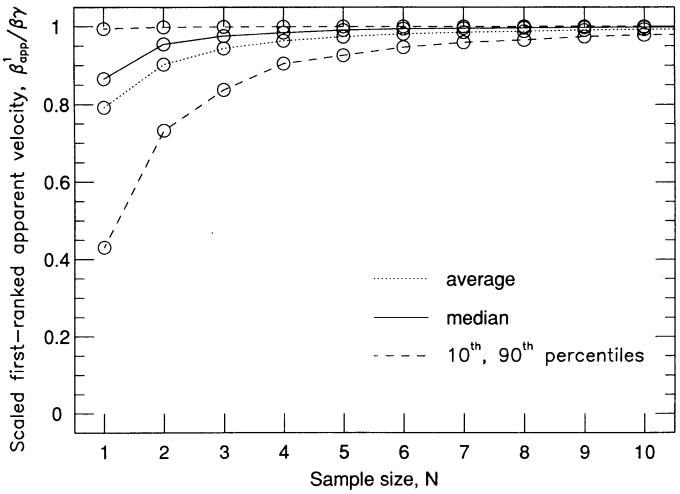

FIG. 13.—Monte Carlo statistics on the first-ranked β_{app} in small samples, for case IIa ($r = 1$). This is a good indicator of likely γ-values, since even in very small samples β^1_{app} almost always lies within a small predictable range, close to the maximum possible $\beta\gamma$.

case IIa model (single γ_b), and with the same bend angle ϕ in each jet, but they do not change in character for more complicated models.

For Figure 12 we first assumed that the bend has a random azimuth with respect to the jet axis at the VLBI core. In that case, in most of the objects the final jet direction will be farther from the line of sight. If $\phi \leq 1/\gamma_b$, then the resultant β_{app} distribution has more high velocities compared with a sample of straight jets. Qualitatively, this occurs because the most likely direction at the core is $\theta \approx 1/(2\gamma_b)$ (Fig. 7), such that a majority of the bends will be toward $\theta = 1/\gamma_b$, where the resultant β_{app} is at the maximum. For $\phi > 1/\gamma_b$, many bends end up past this optimum θ, leading to a predominance of slower β_{app}, characteristic of that angle; for example, if $\phi = 2.5/\gamma_b$, then there will be many $\beta_{app} \approx 0.7\beta_b\gamma_b$, and the cdf will have a characteristic S-shape (Fig. 12). Progressively larger ϕ correspond to progressively lower characteristic β_{app}. Note that, perhaps contrary to one's naive expectations, having a characteristic jet bend angle ϕ results in a rather different predicted β_{app} cdf than having a characteristic ratio r between the pattern velocity and the bulk flow (compare Figs. 8 and 12).

The azimuth of the bend may not be random. In particular, our selection of the brightest jet component favors bends *toward* the line of sight. Since many sources will initially point at $\theta \leq 1/\gamma_b$, bending toward the line of sight leads to a slower β_{app}. A nonrandom azimuth is also part of the helical jet model discussed by Conway & Murphy (1993). Their model needs moderately large bends on parsec scales ($\phi \approx 2.5/\gamma_b$) *away* from the line of sight. In agreement with our Monte Carlo simulations, they predict a predominance of $\beta_{app} \approx 0.7\beta_b\gamma_b$.

3.8. *Apparent Velocity Envelopes in Small Samples*

For a distinctive cdf such as that in case IIa, most of the apparent velocities will be at the high end of the possible range, i.e., near $\gamma_p\beta_p$. This will therefore lead to a well-defined upper envelope to the range of β_{app}, from which the value of γ_p can be read off. We have determined the distribution statistics of the first-ranked apparent velocity (β^1_{app}) in small samples through Monte Carlo simulations. Figure 13 shows the results in terms of scaled β_{app} for case IIa with $r = 1$. In § 5 we will use similar β^1_{app} predictions for more complicated models. Even for a sample size as small as four, we find that, in a large majority of cases, β^1_{app} is very close to the maximum possible ($\gamma_p\beta_p$), as witnessed by the small range of velocity between the 10th and 90th percentiles of the cases found. Therefore, the top-ranked velocity provides a useful diagnostic even for very small samples for core-selected quasars.

Lynden-Bell (1977), Yahil (1979), and Rust, Nash, & Geldzahler (1989) have earlier discussed a similarly powerful analysis method for small samples, but using the *lower* envelope predicted by entirely different and probably untenable superluminal motion models. We believe that, regardless of the model, any lower limits to the β_{app} distribution should be treated with great caution because of observational bias. This applies, for example, to the estimates of H_0 and q_0 by Roland et al. (1993). Similarly, while the lowest velocities in a complete sample of *l*-quasars may reveal interesting information—for example, about a cutoff angle θ_{max}—we will not attempt a quantitative analysis here, since there is at present a heavy selection bias against observing low velocities (see also § 4).

4. ANALYSIS OF THE LOBE-SELECTED QUASARS

In § 2 a set of 13 lobe-selected quasars was defined (*l*-quasars, designated Q*l* in Table 1). These sources come from three complete samples which are likely to be unbiased in the orientation of their radio jets. With such a sample, one has the potential to refute the simple beaming model simply and decisively, if it were found that more than a small fraction of the sources had large β_{app} (e.g., Scheuer 1987). However, for practical reasons, predominantly the brighter *l*-quasars have thus far been selected for VLBI monitoring. These sources should often have their jets pointed closer than average to the line of sight, and thus they should have higher than average β_{app}. Nevertheless, it is clear from the histograms in Figure 3 that the observed values of β_{app} in the *l*-quasars are distributed over a lower range than in the core-selected quasars. Unless the intrinsic properties (e.g., Lorentz factors) of *l*-quasars and *c*-quasars are different, it follows that the *l*-quasars are taken from a much broader range of orientations, in agreement with the standard model. It seems likely that the major impact of the study of *l*-quasars will not be in a quick rejection based on partial results but in the

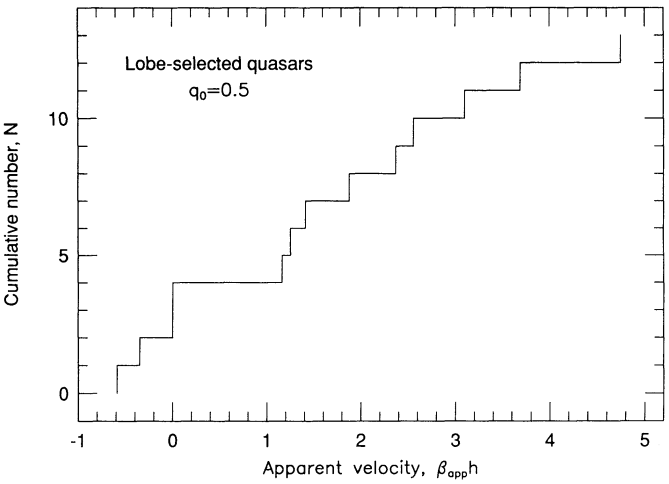

FIG. 14.—Observed cumulative β_{app} distribution for the lobe-selected quasars, assuming $q_0 = 0.5$. Note that preferentially the brighter sources have been observed to date.

derivation of important constraints based on the statistics of complete samples.

Not surprisingly, the observed β_{app} cdf of the *l*-quasars monitored to date, shown in Figure 14, is flatter, with more high velocities, than the predicted cdf for model cases I and III (Fig. 6, discussed in § 3). Note that flattening of the cdf in *l*-quasars cannot result from the fact that different objects probably do not have the same Lorentz factor: Figure 6 demonstrates that, regardless of the Lorentz factor, most of the apparent velocities are predicted to be between 1 and 2 in case I, or between 0 and 1 in case III. The details of the Lorentz factor distribution over the sources affects the shape of the cdf only for the few high values of β_{app}.

In principle, the fact that many β_{app} values in orientation-unbiased samples are predicted to be near a "standard velocity" (which would define a lower envelope in the μ-z diagram) has great potential for cosmology; with objects at both low to moderate redshift and high redshift, one could determine both H_0 and q_0 (e.g., Pelletier & Roland 1989, 1990). However, although the predominant ("standard") velocity range is insensitive to the details of the relativistic Lorentz factor distribution, it may be greatly altered by a least two other effects. First, if, within each source, there is a range including subrelativistic or mildly relativistic Lorentz factors (case III), then, as a result of Doppler favoritism, most β_{app} will be between 0 and 1, rather than between 1 and 2. Second, the "standard range" becomes faster for progressively more severe limiting maximum angles to the line of sight in quasars (θ_{max}), as would apply under quasar and radio galaxy unification hypotheses (see Fig. 11). The interplay of both effects aggravates the uncertainty, since there is a degeneracy between cases I and III in which an almost identical cdf can result for different θ_{max} (see § 3.6 and Fig. 11). This uncertainty is likely to be a significant handicap when attempting to use β_{app} in lobe-selected quasars to determine H_0 and q_0.

The same effects also dictate great care when using β_{app} statistics in *l*-quasars to constrain unification models. For example, an observed distribution with most of the apparent velocities in the range 1–2 could be interpreted under case I to indicate jets pointed completely at random ($\theta_{max} = 90°$), but also under case III to indicate $\theta_{max} = 45°$, if the jets in the sample each have a range of Lorentz factors down to a moderate value of $\gamma_b = \sqrt{2}$ (see eq. [7]). Intermediate θ_{max} would also be possible. A more unambiguous distribution would have a large majority of *sub*luminal β_{app}; this would indicate case III relativistic jets pointed well beyond 45°. This assumes, of course, that there is sufficient evidence to believe that the *l*-quasars, like the *c*-quasars, do have a relativistic jet component, and that the sample is not contaminated by a population with nonrelativistic jets (which would not show superluminal motion in any orientation). Unfortunately, the problem is compounded by the fact that, with different values of H_0, it is rather easy to shift velocities from the range predicted by one hypothesis into that predicted by another hypothesis.

We believe that observational selection effects currently rule out any analysis of the lower end of the β_{app} distribution, and it is clearly too early for a firm interpretation of the statistics of *l*-quasars. However, it is interesting that, already, some of the measured values of β_{app} are very slow, even formally negative, but with 1 σ errors allowing small positive motions. Thus, the observations to date show no indication of a substantial restriction in the angle to the line of sight for quasars. Nevertheless, the occurrence of a lower velocity cutoff, if any, as introduced by the existence of a θ_{max}, is potentially a very powerful diagnostic. It would really come into its own if it could be established, either on theoretical grounds or through high dynamic range image sequences in samples of core-dominated quasars, whether or not a wide range of Lorentz factors occurs within individual jets.

5. ANALYSIS OF THE CORE-SELECTED QUASARS

In § 2 a set of 25 core-selected quasars was defined (*c*-quasars, designated Q*c*'s in Table 1). We assume that they have a strong bias toward jet orientations close to the line of sight, as described by model case II (see § 3). In § 5.1 we first concentrate on the slow or stationary components. In § 5.2 we then discuss a plausible distribution of Lorentz factors to explain the fast motions. An alternative, or perhaps additional explanation, using pattern velocities, is explored in § 5.3. In § 5.4 it is demonstrated how the bulk and pattern Lorentz factors can eventually be disentangled using additional data. Bending in the jets could also affect the β_{app} distribution; this is particularly relevant in view of our selection of the brightest jet component in each source, as discussed in § 5.5. For a statistically meaningful analysis of the β_{app} distribution, we have to use all objects without regard to redshift in these subsections. However, in § 5.6, we use the opposite collapse of the data to one dimension, by analyzing the β_{app} upper envelope as a function of redshift. This procedure is analogous to the often-used method of studying a median observed value as a function of redshift, but makes better use of the fact that the β_{app} distribution is predicted to peak toward high velocities. The analysis reveals a significant difference in the β_{app} statistics between low and high values of q_0, which may affect the interpretation of the β_{app} distribution of $q_0 = 0.05$ as given in §§ 5.2 and 5.3. With many more objects, an analysis similar to the one given here may eventually allow a discrimination between different values of q_0; we comment on the potential cosmological use in § 5.7.

The observed β_{app} cdf in the *c*-quasars is shown in Figure 15 for both $q_0 = 0.05$ and $q_0 = 0.5$. Some of the observed values have large error bars. For example, the one source with a formally negative superluminal motion, 0153+744 (an uncertain member of the *c*-quasars; see § 2.3), has $\beta_{app}h = -5.15$

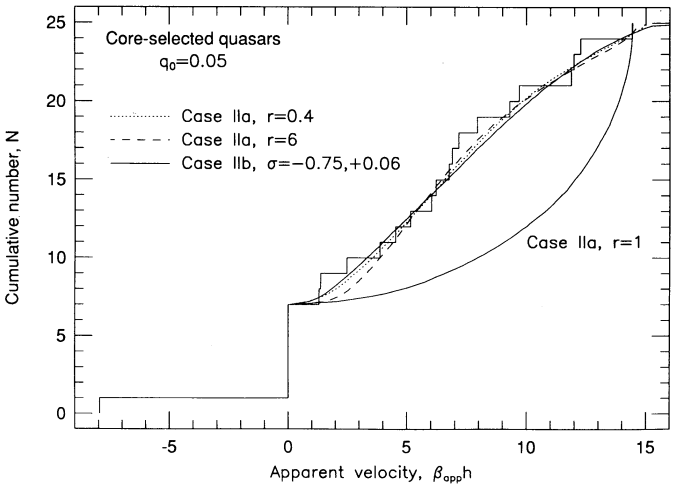

FIG. 15*a*

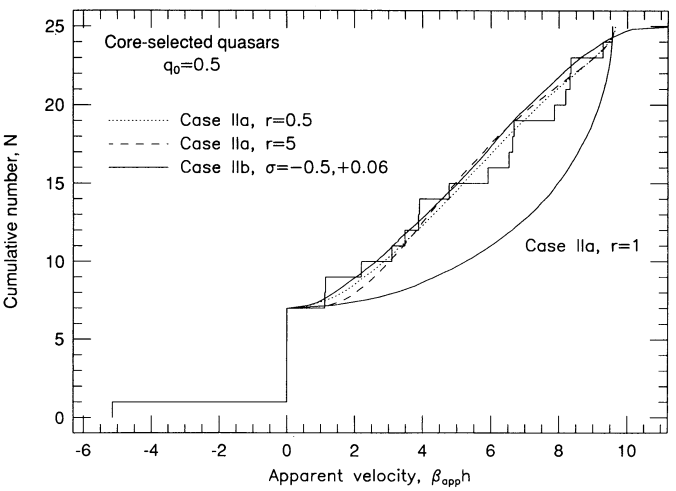

FIG. 15*b*

FIG. 15.—Observed cumulative β_{app} distribution for the core-selected quasars: (*a*) $q_0 = 0.05$; (*b*) $q_0 = 0.5$. Some plausible case IIa and case IIb model curves are shown, as well as case IIa with $r = 1$, which is ruled out. These curves are intended to match only the superluminals, so they are scaled from $\beta_{app} = 0$ at $N = 7$ to the median predicted β^1_{app} at $N = 25$ (see text for details).

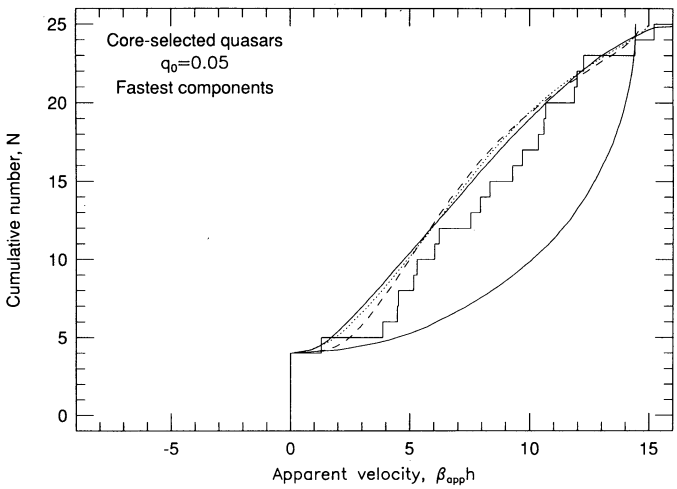

FIG. 16*a*

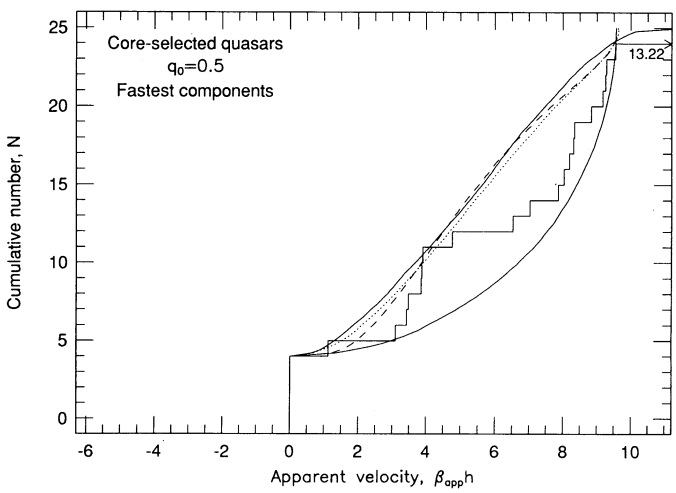

FIG. 16*b*

FIG. 16.—Observed cumulative β_{app} distribution for the core-selected quasars, using the *fastest* rather than the *brightest* components (compare with Fig. 15): (*a*) $q_0 = 0.05$; (*b*) $q_0 = 0.5$. The model curves are not plausible fits but have been copied directly from Fig. 15 without rescaling in apparent velocity, to illustrate the lack of a substantial overall shift toward higher β_{app}, and the larger fraction of β_{app} near the upper envelope.

$\pm$ 9.44 ($q_0 = 0.5$). In this source another (fainter) component has a much more tightly constrained motion, also consistent with zero (see Table 1). However, in other sources β_{app} differs significantly between components. We feel it is important to be as consistent as possible, by always selecting the brightest component for our main analysis (see § 2.2), but since the cdf's obtained with the fastest components are significantly different, and also hint at interesting conclusions (see § 5.5), we show these curves separately in Figure 16.

Histograms of the same β_{app} data are shown in Figure 3. However, with the relatively small number of sources in the sample, comparisons of models with the data are hampered by the arbitrary nature of binning schemes, and we prefer to analyze the cumulative distributions. Of course, it should be kept in mind that the cdf's do not show independent information from point to point. Only a simple analysis is warranted by the current data set, and no formal parameter fitting is attempted. Instead, we discuss a few likely and unlikely Lorentz factor distributions and show representative model cdf curves.

5.1. *Slow and Stationary Components*

There is a sizable number of *c*-quasars in which the brightest jet component has a very small or zero β_{app}, or only an upper limit (seven out of 25). We suspect that in a complete sample the fraction of such sources could be even larger, given the obvious selection against publishing, or even adequately monitoring, slow motions. No distribution of *relativistic* Lorentz factors predicts a significant fraction of motions near zero. Therefore, we suspect that the low β_{app} values do not belong in the same class as the rapid motions, since they cannot be described with the same models. There are too many *c*-quasars with one or more stationary components to dismiss as them as borderline "compact-symmetric" (Qs) sources; the latter category, which we attempted to exclude from the *c*-quasars, seems to have only stationary components (see § 2).

Several explanations for the low values of β_{app} can be considered. First, the jets could genuinely be slow (subrelativistic),

but then they must be intrinsically very luminous to form a substantial fraction of the sample. Second, most of the slow c-quasars could be relativistic, but pointed very close to the line of sight (well within $1/\gamma_b$). However, this requires selection of extremely small angles beyond that introduced by the simple beaming model used in case II (e.g., Fig. 7). Most of the c-quasars were observed as part of radio samples, and we do not know of a satisfactory additional selection mechanism. A non-standard Doppler-boosting index (a very high or very low value of the parameter n or a defined in § 3) could yield a larger number of lower values of β_{app}, but it remains difficult to obtain a significant number of motions near zero (see Fig. 9, § 3.4.2). Third, the motions near zero could indicate patterns from (nearly) stationary shocks in relativistic jets, while the higher β_{app} values could be due to patterns moving relativistically through the bulk flow (see § 5.3). This may be attractive, particularly since some of the sources show both slow and fast components.

5.2. *A Plausible Lorentz Factor Distribution*

In order to explore plausible relativistic Lorentz factor distributions, we will use only the 18 objects with $\beta_{app} > 0$ for the remainder of this subsection. This eliminates one (nonsignificant) negative value, two sources with $\beta_{app} = 0$, and four objects for which only upper limits are available. In order to show the predicted and observed cdf's in the same diagram (Fig. 15), we will place the origin ($\beta_{app} = 0$) for the predicted curves at $N = 7$. Since most models predict a preponderance of large velocities, we have matched the model curves to the data at the high-velocity end (where $N = 25$) by using $\gamma_b h$ as a scale factor. It is derived by requiring that β^1_{app}, the largest of the 18 observed velocities, correspond to the median of the β^1_{app} range obtained in Monte Carlo simulations with samples of 18 objects (see §§ 3.7 and 5.6 for further details on this procedure). With a sample size of 18, the fractional range of β^1_{app} found in the simulations is narrow for all the models discussed, and so the scaling is well determined and internally consistent for each model. We note in passing that the scale factor is the product of the Lorentz factor and H_0, which cannot be measured independently with c-quasars, because, for most plausible models, the shape of the predicted cdf depends almost exclusively on the relative distribution of Lorentz factors and not on their absolute values (see also § 3).

The predicted cdf for case IIa with $r = 1$ ($\gamma_p = \gamma_b$) is drawn in Figure 15. It is a priori unlikely that every source in the universe would have the same Lorentz factor, and the observed range of apparent velocities is indeed much broader than predicted by that simple model. The Kolmogorov-Smirnov test shows only a 0.02% chance that the data have been drawn from the model distribution if $q_0 = 0.05$, and a 1.4% chance if $q_0 = 0.5$.

In a more realistic model, case IIb, the bulk Lorentz factors are allowed to be different between (but not within) sources (see also Murphy 1990). We feel that formal parameter fitting is not warranted, and Figure 15 simply shows representative distributions for $q_0 = 0.05$ and $q_0 = 0.5$. Several different functions can be used, and after some tests we have concluded that a useful characterization of the actual $p(\gamma_b)$ is a skewed Gaussian, in which the upper and lower half-width at half-maximum (HWHM) are different. These two values determine the shape of the predicted β_{app} curve. The value of the central Lorentz factor, on the other hand, determines the relative β_{app} scaling between data and model curves.

While the observed β_{app} distribution has more lower values than predicted for a single Lorentz factor, it does not have a substantial tail of high β_{app}: there is a well-defined upper envelope, which is discussed in § 5.6. This implies that there is a rather sharp upper cutoff to $p(\gamma_b)$. Plausible HWHM values, expressed as a fraction of the central Lorentz factor, are $\lesssim 0.1$ (upper) and ~ 0.5 (lower). Broader distributions seem to be needed for lower q_0. Equating the median predicted β^1_{app} to the observed β^1_{app}, we find that the central Lorentz factor is $\gamma_b \approx 15.0\ h^{-1}$ if $q_0 = 0.05$, and $\gamma_b \approx 9.7\ h^{-1}$ if $q_0 = 0.5$. Given the sharp upper cutoff, the "central" Lorentz factor is in fact quite close to the highest value which can be expected to occur. Note that this analysis was done assuming $r = 1$. Since $r \neq 1$ generally broadens the predicted β_{app} distribution, the estimates given above for the width of $p(\gamma_b)$ are upper limits.

5.3. *Pattern Velocities*

The radio emission seen in VLBI knots is often thought to be due to shocks in the jets. Therefore, it is reasonable to suggest that these knots may not be moving along with the bulk flow but may instead have a separate pattern velocity. In § 3 this possibly was accommodated in case IIa through the ratio $r \equiv \gamma_p/\gamma_b$. As shown in Figure 8, and discussed in § 3.4.2, both $r < 1$ and $r > 2$ lead to a substantial increase in the fraction of slower sources.

Figure 15 illustrates that it is possible to describe the observed β_{app} distribution in the c-quasars quite well by taking only a single γ_b for all sources and also a single value $r \neq 1$. Of course this is implausible, and our analysis only shows likely values of r. Somewhat surprisingly, γ_p could be either larger or smaller than γ_b. The data set does not warrant formal parameter fitting; the observations are well matched with either $r \approx 6$ or $r \approx 0.4$ if $q_0 = 0.05$, and either $r \approx 5$ or $r \approx 0.5$ if $q_0 = 0.5$. Since a realistic $p(\gamma_b)$ (rather than a single value) would broaden the predicted β_{app} distribution, these values of r should be interpreted as extremes, with the actual values likely to be closer to $r = 1$. Of course it is also implausible that the same value of r would apply in all sources; our analysis is only meant to show likely ranges.

Some theoretical estimates indicate a limiting Lorentz factor for a jet advancing into a blackbody radiation field, due to Compton drag, of order $\gamma_b \lesssim 2$–10 (e.g., Phinney 1987; Abramowicz 1992; Henri & Pelletier 1992). With many observed values of $\beta_{app} \approx 10\ h^{-1}$, this suggests that $r > 1$. For example, adopting $h = 0.6$, $\gamma_b \approx 3$ with $r \approx 5$ reproduces the observed β_{app} distribution well for $q_0 = 0.5$. High values of r imply that the patterns would move relativistically through the bulk flow. The physical circumstances under which this could occur are not well known, although it is likely that a significant magnetic field strength is needed (e.g., Jones 1988; Blandford 1990). On the other hand, there is a substantial number of sources with knots in which no motion can be detected. These may indicate that shocks in relativistic jets can also have $r \ll 1$.

5.4. *Disentangling Pattern and Bulk Lorentz Factors*

Figure 15 demonstrates that there are well-fitting models with a single bulk Lorentz factor and either low or high r, and another well-fitting model with a broad distribution of Lorentz factors but $r = 1$ (case IIb, § 5.2). It would not be surprising if the observed β_{app} distribution actually resulted both from a spread in γ_b and from the occurrence of separate pattern velocities. There is in fact an entire family of well-fitting models, which have different combinations of the parameters r and the

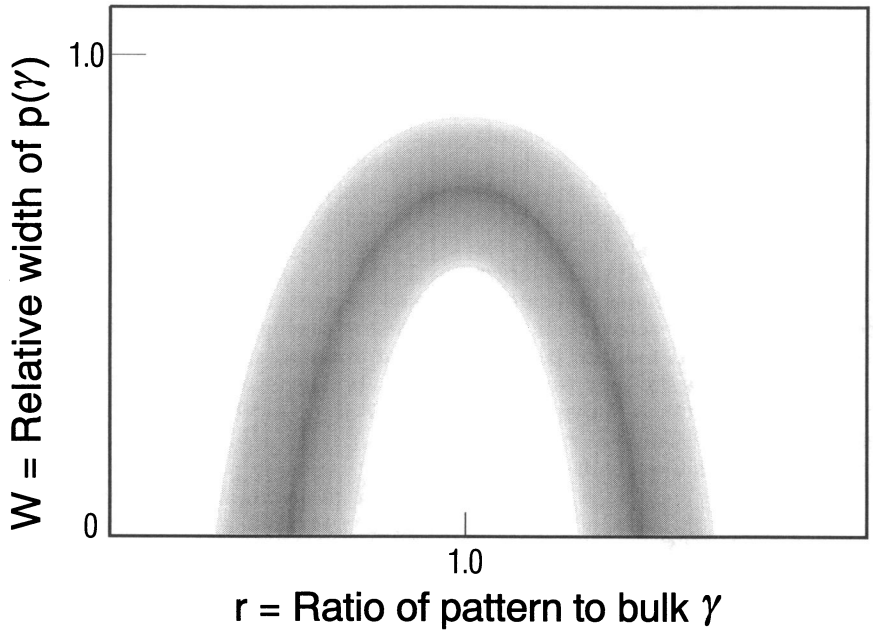

FIG. 17.—Sketch of the locus of plausible values of W (relative γ_b distribution width) and $r \equiv \gamma_p/\gamma_b$ in case IIb (core-selected quasars). We have established that $(r, W) = (0.5, 0)$, $(1, 0.6)$, and $(5, 0)$ are all plausible for $q_0 = 0.5$, and that $(1, 0)$ is excluded (Fig. 15), but a detailed delineation of acceptable parameter values is not warranted by the data, and this sketch is not intended to convey quantitative information.

broadness of $p(\gamma_b)$, which is denoted by W in the sketch of Figure 17. The analysis in §§ 5.2 and 5.3 can be thought of as delineating the extremes in the two parameters, but intermediate models along the curved locus, with values of r closer to unity and a smaller width of $p(\gamma_b)$, are equally likely. It should be stressed that the present data set does not warrant detailed model fitting, and the Figure 17 is not more than the sketch of plausible parameter values. We note again, however, that their locus avoids $(W = 0, r = 1)$: based on the current data, it is unlikely that all sources have the same γ_b without separate pattern velocities.

Ghisellini et al. (1993) have attempted to constrain the Doppler factor (δ) in a large number of sources through the observed deficit of inverse Compton X-ray emission, compared with the predictions based on the radio flux densities. The derived values of δ obviously span a sizable range. Ghisellini et al. (1993) then compare the average Doppler factor, $\langle\delta\rangle$, which is related to the bulk Lorentz factors, with the average apparent velocity in the superluminal sources, $\langle\beta_{app}\rangle$, which is related to the pattern Lorentz factors. They estimate that, if $r > 1$, then $\langle\beta_{app}\rangle \approx 2\langle\delta\rangle$. The assumptions in their paper are closely analogous to our case IIa. However, Figure 18 shows the ratio of $\langle\beta_{app}\rangle$ to $\langle\delta\rangle$ for different r, obtained in Monte Carlo simulations with case IIa. We find that for $r = 1$, $\langle\beta_{app}\rangle \approx 0.6\langle\delta\rangle$. When $r \approx 1.6$, $\langle\beta_{app}\rangle \approx \langle\delta\rangle$, and $\langle\beta_{app}\rangle \approx 2\langle\delta\rangle$ only when $r \approx 4$. These results follow from the fact that core-selected samples have a significant number of sources pointed within $1/\gamma_b$, where δ continues to increase toward $2\gamma_b$, while β_{app} eventually decreases to zero (see also § 3).

We have verified that the values of $\langle\beta_{app}\rangle/\langle\delta\rangle$, while computed for Figure 18 assuming the same bulk Lornetz factor in all sources, do not change greatly for a variety of Lorentz factor distributions in the sample (such as case IIb discussed in § 5.2). Therefore, we believe the distinctive dependence on r could in principle be a tool in the study of superluminals. For example, taking at face value the quantities $\langle\beta_{app}\rangle = 4.4$ and $\langle\delta\rangle = 3.2$, computed by Ghisellini et al. (1993) (with $h = 0.5$ and $n = 3 - \alpha$ in our notation), but using the correctly derived predicted ratios (Fig. 18), it follows that $r \approx 2$, in contradiction to the conclusions of Ghisellini et al. (1993). With $h = 1$, the same procedure indicates $r \approx 1$. We have verified that the ratios in Figure 18 are only weakly dependent on the adopted value of a, so that the comparison is valid for a range of spectral indices, and in particular, for $n = 3 - \alpha$ as chosen by Ghisellini et al. (1993). Note, however, that the Doppler factors calculated by Ghisellini et al. (1993) are lower limits, which become larger for a lower adopted power-law index n (p in their notation); consequently, the derived values of r could be upper limits. However, since the sample used by Ghisellini et

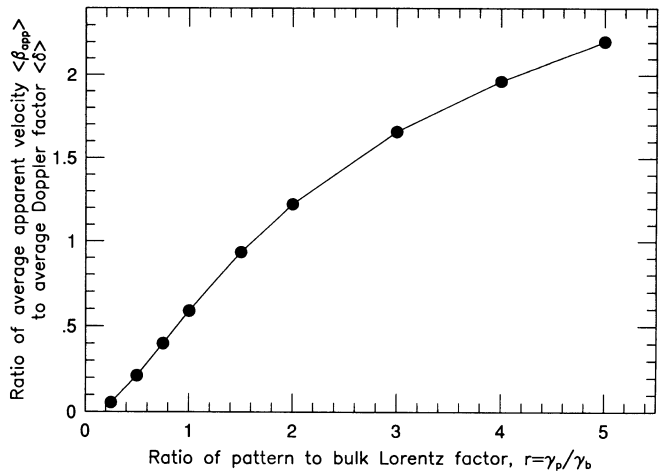

FIG. 18.—Ratio of the average β_{app} to the average Doppler factor δ, obtained under case IIa (core-selected quasars) for different values of r. This observable is in principle a useful tool to determine likely pattern-to-bulk velocity ratios.

al. (1993) is rather less homogeneous than the *c*-quasars we deal with here, and since there are other potential pitfalls in the derivation of Doppler factors (e.g., in the assumed sizes), we believe it is premature to attempt to derive firm constraints on r through a comparison of the currently available Doppler factors and transverse velocities.

The use of averages may introduce biases, and eventually one would also study the full distribution of Doppler factors. Our formalism in § 3 is easily extendable to generate analytical or Monte Carlo predictions of the Doppler factor distribution for various model parameters. In brief trials we have found that, as with β_{app}, different models can produce distinctively different δ cdf curves, but their discussion is outside the scope of this paper. Therefore, we believe it will eventually be possible to determine both the shape of the underlying γ_b distribution and values of r, from a simultaneous analysis of the β_{app} distribution and the distribution of Doppler factors. Several methods of deriving γ_b could be combined, for example inverse Compton arguments (e.g., Ghisellini et al. 1993), radio core-to-lobe flux density ratios R (e.g., Browne & Perley 1986; Murphy 1990; Kapahi & Murphy 1990), fitting of luminosity functions (e.g., Padovani & Urry 1992), rapid variability (e.g., Quirrenbach et al. 1992), or, as recently suggested by Readhead (1994), a comparison of observed brightness temperatures with the equipartition value.

5.5. *Bent Jets*

If there are jets which bend on parsec scales, then our selection of β_{app} in the brightest jet component may favor bends toward the line of sight, and consequently it may favor slower β_{app}, as explained in § 3.7. The data are not sufficiently homogeneous to allow study of correlations between β_{app} and the amount of apparent (projected) bending. However, Figure 16 shows the cdf for the 25 *c*-quasars obtained by selecting the *fastest* rather than the *brightest* component in each source. For comparison, we show the same model predictions as in Figure 15, without changing their velocity scale. Interestingly, the data for the fastest components extend to higher β_{app} than those for the brightest components due to one source (1901+319, 3C 395). Instead, the cdf curves are steeper at the high β_{app} end, particularly if $q_0 = 0.5$, and they show many more β_{app} clustered at large values. This may indicate that the relative width of the $p(\gamma_b)$ distribution (W), and the bulk-to-pattern ratio (r), do not span as wide a range as estimated in the analysis of §§ 5.2 and 5.3 using the brightest components. The locus of plausible values would thus have a smaller radius than sketched in Figure 17.

Conway & Murphy (1993) have suggested the existence of a population of sources in which helically curved jets (initially) bend away from the line of sight. Their model predicted a preponderance of β_{app} values near $\sim 0.7\beta_b\gamma_b$. If the intrinsic $p(\gamma_b)$ distribution is not too wide, this would lead to a characteristically S-shaped cdf (see also § 3.7), which is not seen in the *c*-quasars (Fig. 15). However, we do not have sufficient data to separate out those *c*-quasars with misaligned parsec-scale and kiloparsec-scale jets, which Conway & Murphy (1993) attempted to explain. Since the intrinsic distribution of bulk Lorentz factors, and perhaps pattern velocities, could also have a significant width, many more data will be needed before superluminal motion statistics can serve to constrain such helical jet models. Note that other parts of the model by Conway & Murphy (1993) require $\gamma_b \approx 20$, which they take as evidence either for a very low Hubble constant ($h \approx 0.4$), or for the existence of slow pattern velocities ($r < 1$). Note also that for $q_0 = 0.5$, the cdf of the fastest components (Fig. 16) show a secondary cluster at $\beta_{app} \approx 4\ h^{-1} \approx 0.4\beta^1_{app}$; if this feature persists in large samples, it could be indicative of a bimodal $p(\gamma_b)$, but it could also be related to a characteristic parsec-scale bend angle.

5.6. *Redshift Dependence: The Apparent Velocity Upper Envelope*

There is a fairly well-defined upper envelope in the β_{app}-z diagram (Fig. 2), which is traced out by the core-selected quasars. From Figure 2, the envelope seems to rise as a function of redshift if $q_0 = 0.05$, but it could well be flat if $q_0 = 0.5$. We will quantify the properties of the upper envelope using Lorentz factors derived from first-ranked apparent velocities (β^1_{app}), as explained below; the results are shown in Figure 19. The sample of 25 *c*-quasars is large enough to use β^1_{app} separately in 5 redshift bins, shown along the z-axis. They were chosen to be unequal in extent, in order to obtain five objects in each bin. Since the first-ranked velocity is a property of the bin, each Lorentz factor, though derived from a single velocity, is plotted at the mean redshift of the objects contributing to the bin. We have verified that the basic trend emerges independent of the details of the binning scheme, which is not surprising, since it can also be seen from the full data set in Figure 2.

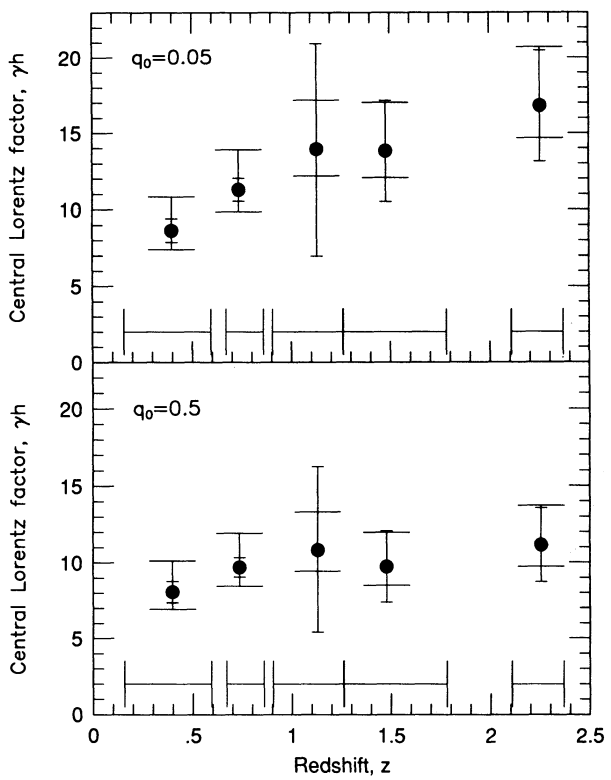

FIG. 19.—Central Lorentz factors as a function of redshift. These indicate likely γ-values, regardless of the detailed distribution of γ. The Lorentz factors increase with z if $q_0 = 0.05$, but they could well be constant if $q_0 = 0.5$. The derivation is based on a comparison of Monte Carlo simulations to the first-ranked observed β_{app} in bins of five objects; the redshift span of each bin is indicated, and the derived γ is drawn at the mean redshift. The error bars with small cross bars at each end correspond to the errors in the individual β^1_{app} measurements; the error bars with large cross bars indicate the statistical uncertainties of our method, for groups of five objects. Further details are given in § 5.6.

Figure 13, discussed in § 3.8, shows the range of β^1_{app} obtained with Monte Carlo simulations, assuming case IIa with $r = 1$ (a single Lorentz factor, and no separate pattern speed). In most samples, even with only a few objects β^1_{app} is close to the maximum possible velocity, $\beta_b \gamma_b$. If there is a range of Lorentz factors, the range of β^1_{app} widens somewhat, but it remains a useful diagnostic, which can be used to derive a Lorentz factor by assuming that in each bin the *observed* β^1_{app} is at the median of the *predicted* range, which is fixed in terms of $\beta_b \gamma_b$. We have adopted a skewed Gaussian $p(\gamma_b)$ with a fixed upper HWHM of 0.06 and lower HWHM of 0.5 under case IIb (see § 5.2 and Fig. 15) to obtain self-consistent central Lorentz factors in each redshift bin; they are shown in Figure 19. In order to derive the approximate equivalent of 1 σ error bars on the central Lorentz factors, we have used the interval between the 16.7th and 83.3d percentiles of the predicted β^1_{app} range. These uncertainties, related to the small-number statistics, are shown in Figure 19 as error bars with large horizontal ends. Note that they are asymmetric, allowing more uncertainty toward larger Lorentz factors than toward smaller ones. We emphasize that, while we have defined the large error bars such that there is approximately a two-thirds chance that the actual central Lorentz factor is in the range shown, the likelihood of values progressively farther outside the range decreases much more rapidly than under Gaussian statistics. We also show the measurement uncertainties derived from the individual β^1_{app} observations as error bars with small horizontal ends. Many of these measurement errors are comparable to the estimated statistical uncertainties. Note finally that the derived Lorentz factors, like the apparent velocities, scale with h^{-1}.

With equal numbers of objects per bin, the same conversion factor from β^1_{app} to γ_b is used throughout, and the conversion then neither obscures nor creates any dependence of the derived central Lorentz factors on redshift. Moreover, the values and their statistical error bars are insensitive to the kind of model adopted for the Monte Carlo upper envelope predictions. It is only required that the model chosen predicts a β_{app} cdf which approximately matches the data. Thus the effects of $r \neq 1$ models on the γ_b-z diagram are well represented by Figure 19, although that was computed with another model. Furthermore, even the use of models which do not reproduce the observed cdf well would to first order not introduce a spurious change of slope with redshift but would cause the derived central Lorentz factors to be systematically biased. In general, it is easy to see that, when using β^1_{app}, an underestimate of the broadness of $p(\gamma_b)$ will result in an underestimate of the central Lorentz factor. The results might, however, be skewed if there were evidence in the data for a significant change in the *shape* of the underlying $p(\gamma_b)$ between redshift bins. The sample of 25 *c*-quasars is too small to allow a meaningful study of the complete distribution of apparent velocities in individual redshift bins. However, high and low β_{app} seem to occur in similar proportions in all redshift bins, and there is no evidence that changes in the shape of $p(\gamma_b)$ with redshift seriously affect our procedure.

We emphasize again that, qualitatively, the redshift dependence shown in Figure 19 is visible directly in the *observed* β_{app} (Fig. 2), independent of any analysis method. Furthermore, the results are insensitive to our use of β_{app} measured in the brightest component of each source; Cohen & Vermeulen (1992) found a qualitatively similar result in a (less rigorous) analysis using the *fastest* component in each source. It is also important to note that luminosity data for a substantial fraction of the *c*-quasar sample (Herbig & Readhead 1992) show no evidence that the observed increase of β^1_{app} with z for $q_0 = 0.05$ is imposed by any correlation of β_{app} with luminosity. We also do not know of observational selection effects which could cause the correlation. For example, it becomes more difficult to measure low β_{app} at higher z, but the high β_{app} values near the upper envelope can be measured at all z. Finally, although the *c*-quasars are not really a complete, flux-limited sample, the upper envelope is unlikely to be affected, since mostly low-β_{app} objects will be missing.

We believe it is plausible to express any change of the central Lorentz factor with redshift in the traditional form as proportional to $(1 + z)^s$. Formal least-squares fits, weighted with the statistical and measurement errors added in quadrature, yield $s = 0.72 \pm 0.36$ for $q_0 = 0.05$, and $s = 0.27 \pm 0.36$ for $q_0 = 0.5$. Thus, for a closed universe there is no evidence for evolution of the Lorentz factors, while if the universe is open we have found an indication that Lorentz factors increase with redshift. This implies that, if $q_0 = 0.5$, there is no problem in combining data from a wide range in redshift in order to study the cdf, while if $q_0 = 0.05$, it may cause the β_{app} distribution to appear flattened ("smeared out"). In that respect, it is interesting that the cdf for $q_0 = 0.05$ (both for the brightest and for the fastest components) indicate wider $p(\gamma_b)$, or more extreme r, than the equivalent curves computed assuming $q_0 = 0.5$.

On the assumption that evolution of the Lorentz factors in parsec-scale jets is unlikely, the result could be turned into the conclusion that the universe is not far from closed ($q_0 \approx 0.5$; see also § 5.7). However, there are a number of potential biases, and the *c*-quasars do not form a true core-selected, flux-limited sample. Therefore, such statements about the geometry of the universe are at present not warranted. We do, however, feel that the sample is sufficiently large, homogeneous, and well distributed in redshift that the intriguing trends seen in Figure 18 merit serious attention and a dedicated effort to increase the sample statistics.

5.7. *Cosmology with Core-selected Quasars*

The statistical distribution of Lorentz factors observed on parsec scales is a property of quasars which, one hopes, might show little cosmological evolution. It is determined by astrophysical processes in the nuclear region only, and consequently is unlikely to change as a result of changing environmental conditions on galactic and intergalactic scales. Similar arguments have been applied for the use of the parsec-scale size of radio-loud quasars as a standard rod (e.g., Kellermann 1993). However, it is not clear to us how the angular-size–redshift method is affected by orientation effects, and by changes in optical depth, particularly as a function of emitted wavelength. Conversely, there is no statistical evidence to suggest that VLBI component motions are systematically faster or slower depending on the emitted or observed wavelength; some sources have been studied at numerous wavelengths. Thus, we have the real hope that superluminal motion studies will yield the derivative of the standard rod: a standard β_{app} distribution, for use as a cosmological probe.

The initial goal would be to obtain a sample of at least 25 objects, but rather more homogeneous both in selection method and in measurement method than the current *c*-quasar sample. With these, one might take the current β^1_{app} analysis one step further and derive the value of q_0 for which the "evolution" power-law index s (defined in § 5.6) is zero, and the interval around it in which s is within 1 σ of zero. However,

superluminal motion statistics with core-selected objects will become a much more powerful tool once sufficiently large homogeneous samples are available to study the full β_{app} distribution in separate redshift bins. This will first of all be of great interest for jet astrophysics; combined with morphological data, Doppler factors, and core-to-lobe flux density ratios, there are good prospects for making useful contraints on the distribution of both bulk and pattern Lorentz factors. Second, it would then be possible to constrain q_0 with much more confidence. It may then be found that, despite our hopes, the distribution of Lorentz factors evolves. However, with well-determined distributions in sufficiently many bins spread out in redshift, it is possible that evolution can be disentangled from an unphysically stretching of the β_{app} distribution caused by the "wrong" choice of q_0 in the analysis. We believe that for these important goals it would be both desirable and feasible to obtain apparent velocity measurements in a sample of approximately 200 objects over the next 5 years, and efforts to achieve this are currently underway using snapshot VLBI techniques on the newly available VLBA and global networks.

6. SUMMARY

The first part of this paper (§ 2) is an up-to-date compilation of internal proper motion measurements and upper limits in extragalactic radio sources, with a discussion of the data reliability and uniformity. The second part (§ 3) presents the predicted β_{app} distributions for several relativistic beaming model variants, and demonstrates the effects of pattern velocities (distinct from the bulk flow), of bending, and of a cutoff in the distribution of jet directions. In the third part, §§ 4 and 5, we then use the model predictions to study the observed β_{app} distributions in lobe-selected and core-selected quasars. The core-selected group is now large enough to have intriguing implications both for the astrophysics of relativistic jets and for cosmological studies. The analysis of the current sample was used in part to point out how superluminal motion studies of larger samples may yield important results in the coming years. Our principal conclusions can be summarized as follows:

1. The β_{app} distribution for core-selected quasars depends on the value of q_0. There is an upper envelope in the β_{app}-z diagram. It rises with z if $q_0 = 0.05$, but it could well be flat if $q_0 = 0.5$. This can be quantified by assuming a γ_b distribution with a central value proportional to $(1 + z)^s$. Use of the predictive power of first-ranked β_{app} in very small samples yields $s = 0.72 \pm 0.36$ for $q_0 = 0.05$, and $s = 0.27 \pm 0.36$ for $q_0 = 0.5$. The result is insensitive to the details of the assumed γ_b distribution. Our analysis illustrates that *the β_{app} statistics of a sufficiently large complete sample of core-selected quasars can be used to constrain q_0*. First, the β_{app}-z upper envelope may be used as a "standard velocity" by assuming that this property of the nuclear regions of quasars does not evolve. Eventually, it will be possible to study the complete β_{app} distribution, rather than just the upper envelope, as a function of redshift. Much firmer constraints may then be placed on q_0 from the requirement that evolution of the β_{app} distribution, if any, should have a physically plausible form.

2. In core-selected samples, pattern and bulk Lorentz factors both play a role in determining the β_{app} distribution; we define $r \equiv \gamma_p/\gamma_b$. The largest fraction of fast β_{app} occurs for $r \simeq 1.5$; slow ($r < 1$) and fast ($r > 2$) patterns both lead to a larger fraction of relatively slow β_{app}. *The data on the core-selected quasars rule out the possibility that they all have the same Lorentz factor and* $r = 1$. Their superluminal velocity distribution can, however, be fitted well with a single γ_b in all sources, if there are either slow patterns ($r \simeq 0.5$) or fast patterns ($r \simeq 5$). An alternative fit has $r = 1$, but a wide γ_b distribution over the sources (relative width $W \geq 0.5$). The γ_b distribution must be skewed to favor high γ_b by having a sharp upper cutoff and a more gradual tapering off toward lower γ_b. It is plausible that both a range of γ_b and separate pattern velocities are present: as sketched in Figure 17, many intermediate (W, r) combinations are possible, but the locus does not include (0, 1).

3. The core-selected quasars contain the highest β_{app}; the group defines the upper envelope in the μ-z and β_{app}-z diagrams. However, although there is a larger fraction of high β_{app} than in the other groups, in $\sim 30\%$ of the core-selected quasars the brightest jet component is stationary to within the measurement errors. These slow components are likely to be underrepresented in the currently published data. Stationary and moving knots sometimes coexist in the same source. The stationary knots may be due to shocks with $r \ll 1$; they cannot be explained well together with the faster sources in a single, smooth distribution of bulk and pattern Lorentz factors.

4. The β_{app} and R data for the different object categories are in general agreement with AGN unification models but, given their inhomogeneity, do not support or constrain those models strongly. Superluminal motion might be completely absent in GPS sources.

5. Our models show that in samples selected on beamed emission, the relative β_{app} distribution is insensitive to the absolute γ_b values. There is a large fraction of β_{app} just below the *maximum* possible, $\gamma_b \beta_b$; the fraction gets smaller for a wider relative range of γ_b over the sample. Conversely, randomly oriented samples are predicted to have a preponderance of low β_{app} just above the *minimum* β_p. In this case the predicted β_{app} distribution is insensitive to the distribution of faster Lorentz factors in the sample.

6. We have investigated the effect of a possible internal spread of Lorentz factors in individual jets, assuming that Doppler favoritism then selects which value is observed. In randomly oriented samples, the predominant β_{app} values are strongly dependent on what the lowest (possibly only mildly relativistic) γ_b values in the range are. On the other hand, the β_{app} distribution in core-selected quasars is insensitive to such an internal γ_b spread, and core-selected samples cannot be used as an indicator for it. We also find that Doppler favoritism is not a good γ_b selection mechanism at small angles to the line of sight. Therefore, the fact that superluminal components are generally seen to move as discrete entities is an argument against the existence of a wide internal range of γ_b.

7. An upper cutoff in the distribution of angles to the line of sight, as appropriate for quasars in some unification models, has little effect on the predicted β_{app} distribution for core-selected samples but strongly increases the predominant β_{app} values in randomly oriented (lobe-selected) samples. However, it will be difficult to constrain any cutoff angle, even with a complete sample of lobe-selected quasars, if it is unknown whether or not the jets have a broad internal range of γ_b, because there is a degeneracy between the predictions for specific maximum quasar angles to the line of sight and specific minimum γ_b. Uncertainty in the value of H_0 aggravates the problem.

8. Attempts to find a "standard velocity" in lobe-selected quasars, to determine H_0 and q_0, are similarly hampered by

the uncertainty over the value of a possible maximum quasar angle to the line of sight, and the possible existence of a wide range of Lorentz factors within each jet.

9. If jets bend through a modest angle $\phi \leq 30°$ between the core and the moving VLBI knot, this has little effect on the predicted β_{app} distribution for randomly oriented samples. For core-selected quasars, different results are possible. If the azimuth is random, bends of $\phi \leq 1/\gamma_b$ lead to a larger number of high values of β_{app} than for straight jets, but progressively larger bends lead to a predominance of progressively lower values of β_{app}. Bends could be preferentially toward the line of sight—for example, due to the selection of the brightest components—or they could be preferentially away from the line of sight, as in the helical jet model of Conway & Murphy (1993); in both cases there are fewer of the highest velocities, compared to straight jets, but the detailed β_{app} distributions differ.

10. If, in the observed core selected quasars with multiple components, the fastest rather than the brightest one is selected, the resultant β_{app} distribution does not significantly extend to higher velocities but instead has a larger fraction of values near the upper envelope. This signature conforms to the predictions for bent jets, and may indicate that the parameters W and r of the Lorentz factor distribution may have a less extreme range than indicated in point 2 and Figure 17.

11. Monte Carlo predictions of $\langle\beta_{app}\rangle/\langle\delta\rangle$, where δ is the Doppler factor (e.g., from inverse Compton considerations; see also Ghisellini et al. 1993), show that this ratio is in principle a useful indicator for typical values of r in core-selected quasars, and is insensitive to the detailed γ_b distribution. Our β_{app} distribution prediction formalism can be extended to δ, and, since different beaming model parameters can give distinctively different δ distributions, we believe it will eventually be possible to determine both the width W of the underlying γ_b distribution and the values of r.

12. Since, in core-selected samples, many β_{app} are predicted to be just below the maximum possible value, the upper envelope should be well defined. Even in very small samples the largest observed β_{app} is a good indicator of likely Lorentz factors. Monte Carlo simulations can be used for quantitative estimates, as was done for our estimates of the dependence of γ on the value chosen for q_0 (see point 1).

We are indebted to many of our colleagues at Caltech for stimulating discussion on the subject of superluminal motion statistics. We are particularly grateful to Tim Pearson for his comments on an earlier version of the manuscript, to Tony Readhead for some useful suggestions, and to Charles Lawrence for supplying and correcting some redshifts. We have also benefited from discussions, and a comparison of object lists, with Ken Kellermann. We thank Paolo Padovani for remarks which have led us to sharpen the discussion of the use of Doppler factors. This work has been supported by the National Science Foundation under grants AST 88-14554 and AST 91-17100.

APPENDIX

To calculate β_{app} distributions, we first need to compute $p(\theta, \gamma_p)$, the simultaneous probability density function (pdf) for the angle to the line of sight and the pattern Lorentz factor. For samples selected on beamed emission, this must be $p(\theta, \gamma_p | S)$, the pdf conditional on a given observed flux density S, but it will be shown that for power-law source counts (eq. [6]) the result is independent of S. The apparent velocity pdf, $p(\beta_{app})$, must then be derived using equation (2), which relates β_{app} to θ and γ_p. However, since β_{app} is not a monotonic function of θ, the cumulative distribution function (cdf), $P(\beta'_{app} \leq \beta_{app})$, must be computed first.

For cases I and II, θ and γ_p are independent, and we have

$$P(\beta'_{app} \leq \beta_{app}) = 1 - P(\beta'_{app} > \beta_{app}) = 1 - \int_{\gamma_{p,l}(\beta_{app})}^{\gamma_{p,u}(\beta_{app})} d\gamma_p \int_{\theta_l(\beta_{app},\gamma_p)}^{\theta_u(\beta_{app},\gamma_p)} d\theta\, p(\theta, \gamma_p)\,. \tag{A1a}$$

From a consideration of equation (2) it can be shown that the integration limits are

$$\begin{aligned}
\gamma_{p,l}(\beta_{app}) &= \begin{cases} \gamma_{p,\min}\,, & \beta_{app} \leq \beta_{p,\min}\gamma_{p,\min}\,, \\ (\beta_{app}^2 + 1)^{1/2}\,, & \beta_{app} \geq \beta_{p,\min}\gamma_{p,\min}\,, \end{cases} \\
\gamma_{p,u}(\beta_{app}) &= \gamma_{p,\max} \qquad \forall\, \beta_{app}\,, \\
\cos\theta_l(\beta_{app}, \gamma_p) &= \frac{\beta_{app}^2 + D}{\beta_p(\beta_{app}^2 + 1)} \qquad \forall\, \beta_{app}\,, \\
\cos\theta_u(\beta_{app}, \gamma_p) &= \begin{cases} 0\,, & \beta_{app} \leq \beta_p\,, \\ \dfrac{\beta_{app}^2 - D}{\beta_p(\beta_{app}^2 + 1)}\,, & \beta_{app} \geq \beta_p\,, \end{cases}
\end{aligned} \tag{A1b}$$

where we have defined

$$D(\beta_{app}, \gamma_p) \equiv (\beta_{app}^2\beta_p^2 + \beta_p^2 - \beta_{app}^2)^{1/2} = \beta_p\left[1 - \left(\frac{\beta_{app}}{\beta_p\gamma_p}\right)^2\right]^{1/2}\,. \tag{A1c}$$

Note that for reasonably large Lorentz factors ($\gamma_p > 2$), the function D depends almost exclusively on the *scaled* apparent velocity ($\beta_{app}/\beta_p\gamma_p$); the functional form is thus independent of the Lorentz factor.

For cases III and IV, the value of $\gamma_p = \gamma_b$ is fixed for given θ, so that only $p(\theta)$ and $p(\theta \mid S)$ remain, and equation (2) is replaced by equation (8). Instead of equation (A1), we have

$$P(\beta'_{\rm app} \leq \beta_{\rm app}) = 1 - \int_{\theta_l(\beta_{\rm app})}^{\theta_u(\beta_{\rm app})} d\theta\, p(\theta)\,, \tag{A2a}$$

where the integration limits follow from equation (8) as

$$\cos\,\theta_l(\beta_{\rm app}) = \frac{\beta_{\rm app}^2 + D_m}{\beta_{p,\max}(\beta_{\rm app}^2 + 1)} \qquad \forall\ \beta_{\rm app},$$

$$\tan\,\theta_u(\beta_{\rm app}) = \frac{1}{\beta_{\rm app}} \qquad \forall\ \beta_{\rm app}\,, \tag{A2b}$$

with

$$D_m \equiv D(\beta_{\rm app},\, \gamma_p = \gamma_{p,\max})\,. \tag{A2c}$$

If desired, differentiation of equation (A1) or equation (A2) then gives the final differential $\beta_{\rm app}$ distribution:

$$p(\beta_{\rm app})d\beta_{\rm app} = \frac{d}{d\beta_{\rm app}}\,[P(\beta'_{\rm app} \leq \beta_{\rm app})]d\beta_{\rm app}\,. \tag{A3}$$

For all but the simplest models, the full analytical derivations of $P(\beta_{\rm app})$ become intractable. Instead, many cdf's shown in this paper were derived through Monte Carlo simulations, for which it is sufficient to have computed $p(\theta, \gamma_p)$, such that a set of θ and γ_p values can be drawn at random from this distribution, to generate a population of sources. For each source, $\beta_{\rm app}$ can then be computed with equation (2) or equation (8), such that the distribution of $\beta_{\rm app}$ can be studied for this synthetic population.

A1. CASE I: SINGLE LORENTZ FACTOR; RANDOM JET ANGLES

Since in case I there is no selection on beamed emission, the simultaneous pdf for θ and γ_p is just the product of their individual pdf's. If all sources have the same pattern Lorentz factor, $\gamma_{p,f}$ then, using equation (3), we have

$$p(\theta, \gamma_p)d\theta\, d\gamma_p = \sin\,\theta\,\delta(\gamma_p - \gamma_{p,f})d\theta\, d\gamma_p\,. \tag{A4}$$

With equation (A1), and denoting

$$D_f \equiv D(\beta_{\rm app},\, \gamma_p = \gamma_{p,f})\,, \tag{A5}$$

we then find

$$P(\beta'_{\rm app} \leq \beta_{\rm app}) = \begin{cases} 1 - \dfrac{\beta_{\rm app}^2 + D_f}{\beta_{p,f}(\beta_{\rm app}^2 + 1)}\,, & \beta_{\rm app} \leq \beta_{p,f}\,, \\ 1 - \dfrac{2D_f}{\beta_{p,f}(\beta_{\rm app}^2 + 1)}\,, & \beta_{\rm app} \geq \beta_{p,f}\,. \end{cases} \tag{A6}$$

From equation (A3), the differential distribution is

$$p(\beta_{\rm app})d\beta_{\rm app} = \begin{cases} \dfrac{\beta_{\rm app}}{D_f\,\beta_{p,f}(\beta_{\rm app}^2 + 1)}\left[\dfrac{2(1 - D_f)}{\beta_{\rm app}^2 + 1} + \beta_{\rm app}^2 - 1\right]d\beta_{\rm app}\,, & \beta_{\rm app} < \beta_{p,f}\,, \\ \dfrac{2\beta_{\rm app}}{D_f\,\beta_{p,f}(\beta_{\rm app}^2 + 1)}\left[\dfrac{2}{\beta_{\rm app}^2 + 1} + \beta_{\rm app}^2 - 1\right]d\beta_{\rm app}\,, & \beta_{\rm app} > \beta_{p,f}\,. \end{cases} \tag{A7}$$

It may be useful to point out that $p(\beta_{\rm app} = \beta_{p,f}\gamma_{p,f}) = \infty$, since in the denominator $D(\beta_{\rm app} = \beta_{p,f}\gamma_{p,f}) = 0$ (see eq [A1c]). This corresponds to a slight upturn at high $\beta_{\rm app}$ in the cdf (eq. [A6]; see Fig. 6*a*), which is due to the fact that $\beta_{\rm app}(\theta)$ is flat at the maximum $\beta_{\rm app}$ (eq. [2] is a continuously differentiable function).

A2. CASE II: SINGLE LORENTZ FACTOR; DOPPLER BOOSTING ORIENTATION BIAS

If sources are selected on emission dominated by Doppler boosting,then the simultaneous pdf $p(\theta, \gamma_p)$, will depend on the flux density of the observed source; we have $p(\theta, \gamma_p \mid S_{\rm obs})$. This must be computed from its inverse, $p(S_{\rm obs} \mid \theta, \gamma_p)$, the probability of finding a source of flux density $S_{\rm obs}$ given θ and γ_p. First, with the known Doppler boosting process, described by equation (5), and with given differential source counts (eq. [6]), one can compute $p(S_{\rm obs} \mid \theta, \gamma_b)$, which depends on the *bulk* rather than the pattern Lorentz factor. If one jet dominates the total flux density observed from any source (assumption 2), then, for a fixed $S_{\rm obs}$, it can be seen from equation (5) that

$$\begin{aligned} S_{t,\min} &= (1 - \beta_{b,\max})^n S_{\rm obs} \qquad &&(\text{when } \theta = 0)\,, \\ S_{t,\max} &= S_{\rm obs} \qquad &&\left(\text{when } \theta = \frac{\pi}{2}\right). \end{aligned} \tag{A8}$$

Therefore,

$$p(S_{\rm obs}\,|\,\theta,\,\gamma_b)dS_{\rm obs} = p[S_t = (1-\beta_b\cos\theta)^n S_{\rm obs}]dS_t$$
$$= \frac{[(1-\beta_b\cos\theta)^n S_{\rm obs}]^{-(q+1)}}{q\{[(1-\beta_{b,\rm max})^n S_{\rm obs}]^{-q} - S_{\rm obs}^{-q}\}}(1-\beta_b\cos\theta)^n dS_{\rm obs}$$
$$= \frac{1}{qS_{\rm obs}}\frac{(1-\beta_b\cos\theta)^{-nq}}{(1-\beta_{b,\rm max})^{-nq}-1}dS_{\rm obs}\,. \tag{A9}$$

Note that the exponents depend on n and q only in their product. We will define

$$a \equiv nq - 1\,. \tag{A10}$$

For completeness, we note that including in equation (A9) the contribution of the receding jet to the total observed flux density would lead to

$$p(S_{\rm obs}\,|\,\theta,\,\gamma_b)dS_{\rm obs} = \frac{1}{qS_{\rm obs}}\frac{[(1-\beta_b\cos\theta)^{-n}+(1+\beta_b\cos\theta)^{-n}]^q}{[(1-\beta_{b,\rm max})^{-n}+(1+\beta_{b,\rm max})^{-n}]^q - 2^q}dS_{\rm obs}\,, \tag{A11}$$

which can be further analyzed numerically only after choosing values for n and q. In our final analytically derived cdf there is a very slight shortage of the slowest velocities. Note also that, conversely, a model with completely one-sided jet sources (cf. Cohen 1989), which can also be investigated analytically, would yield a very slight excess of the slowest velocities, from receding jets which would be outshone by the approaching counterpart if jets are two-sided.

Equation (A9) can be formally inverted with

$$p(\theta,\,\gamma_b\,|\,S_{\rm obs})d\theta\,d\gamma_b = \left[p(S_{\rm obs}\,|\,\theta,\,\gamma_b)p(\theta)p(\gamma_b)\Big/\int_{\gamma_{b,\rm min}}^{\gamma_{b,\rm max}}d\gamma_b\,p(\gamma_b)\int_0^{\pi/2}d\theta\,p(\theta)p(S_{\rm obs}\,|\,\theta,\,\gamma_b)\right]d\theta\,d\gamma_b\,. \tag{A12}$$

Using equation (3) to perform the integration over θ yields, for $a \neq 0$,

$$p(\theta,\,\gamma_b\,|\,S_{\rm obs})d\theta\,d\gamma_b = \left\{a(1-\beta_b\cos\theta)^{-a-1}\sin\theta\Big/\int_{\gamma_{b,\rm min}}^{\gamma_{b,\rm max}}d\gamma_b\,p(\gamma_b)\frac{1}{\beta_b}[(1-\beta_b)^{-a}-1]\right\}d\theta\,p(\gamma_b)d\gamma_b\,. \tag{A13}$$

Note that $S_{\rm obs}$ no longer appears in equation (A13). Thus,

$$p(\theta,\,\gamma_b\,|\,S_{\rm obs}) = p(\theta,\,\gamma_b)\,. \tag{A14}$$

This is a result of assuming a selection on purely Doppler-boosted emission from a population with differential source counts which obey a single power law over a wide range (eq. [6], eq. [A9]); Urry & Shafer (1984) reached analogous conclusions regarding the transformation of luminosity functions by Doppler beaming.

We will proceed with the analytical derivation only for the simple situation where all sources have the same bulk Lorentz factor, $\gamma_{b,f}$. This variant will be called case IIa. The integration in equation (A13) over the bulk Lorentz factors is now trivial:

$$p(\theta)d\theta = \frac{a\beta_{b,f}(1-\beta_{b,f}\cos\theta)^{-a-1}\sin\theta}{(1-\beta_{b,f})^{-a}-1}d\theta\,. \tag{A15}$$

The equivalent expression assuming one-sided jets was given by Cohen (1989).

In § 5 we also use a more general variant, called case IIb, with a distribution of bulk Lorentz factors, $p(\gamma_b)$. All distributions were truncated at $\gamma_b = 2$, below which our relativistic model approximations are no longer valid; such low Lorentz factors do not produce much beaming, and hence we do not expect many of these in the core-selected quasars. A given $p(\gamma_b)$ can be investigated through Monte Carlo simulations, by first selecting, for each object, a bulk Lorentz factor from the given distribution. This makes the step from equation (A13) to equation (A15). Then an angle to the line of sight can be drawn from its own distribution, which depends on the γ_b previously drawn.

Using equation (A1), and assuming a one-to-one relationship between the pattern and bulk Lorentz factors (see eq. [4]), the cdf for the apparent velocities in case IIa is

$$P(\beta'_{\rm app}\le\beta_{\rm app}) = \begin{cases} 1-\left[\left(1-\dfrac{\beta_{b,f}}{\beta_{p,f}}\dfrac{\beta_{\rm app}^2+D_f}{\beta_{\rm app}^2+1}\right)^{-a}-1\right][(1-\beta_{b,f})^{-a}-1]^{-1}\,, & \beta_{\rm app}\le\beta_{p,f}\,, \\ 1-\left[\left(1-\dfrac{\beta_{b,f}}{\beta_{p,f}}\dfrac{\beta_{\rm app}^2+D_f}{\beta_{\rm app}^2+1}\right)^{-a}-\left(1-\dfrac{\beta_{b,f}}{\beta_{p,f}}\dfrac{\beta_{\rm app}^2-D_f}{\beta_{\rm app}^2+1}\right)^{-a}\right][(1-\beta_{b,f})^{-a}-1]^{-1}\,, & \beta_{\rm app}\ge\beta_{p,f}\,, \end{cases} \tag{A16}$$

with D_f given by equations (A5) and (A1c). If the bulk and pattern speeds are equal ($r = 1$), equation (A16) simplifies to

$$P(\beta'_{\rm app}\le\beta_{\rm app}) = \begin{cases} 1-\dfrac{(1+D_f)^a-(1-\beta_{p,f}^2)^a}{(1+\beta_{p,f})^a-(1-\beta_{p,f}^2)^a}\,, & \beta_{\rm app}\le\beta_{p,f}\,, \\ 1-\dfrac{(1+D_f)^a-(1-D_f)^a}{(1+\beta_{p,f})^a-(1-\beta_{p,f}^2)^a}\,, & \beta_{\rm app}\ge\beta_{p,f}\,. \end{cases} \tag{A17}$$

A3. CASE III: LARGE RANGE OF LORENTZ FACTORS; RANDOM JET ANGLES

Without selection of the sample sources on beamed emission, the distribution of angles to the line of sight is directly given by equation (3). Using equation (A2), and adopting the same $\gamma_{p,\max}$ in all sources, therefore yields

$$P(\beta'_{\rm app} \le \beta_{\rm app}) = 1 + \frac{\beta_{\rm app}}{(1+\beta_{\rm app}^2)^{1/2}} - \frac{\beta_{\rm app}^2 + D_m}{\beta_{p,\max}(\beta_{\rm app}^2+1)} . \tag{A18}$$

A4. CASE IV: LARGE RANGE OF LORENTZ FACTORS; DOPPLER-BOOSTING ORIENTATION BIAS

The probability of finding a boosted flux density $S_{\rm obs}$ for given θ and γ_b is analogous to case II (see eq. [A9]); with the selection of the most favorable Lorentz factor for a given angle (eq. [A7]), one then obtains

$$p(S_{\rm obs}\,|\,\theta)dS_{\rm obs} = \begin{cases} \dfrac{1}{qS_{\rm obs}} \dfrac{(1-\beta_{b,\max}\cos\theta)^{-a-1}}{(1-\beta_{b,\max})^{-a-1}-1}\, dS_{\rm obs} , & \cos\theta \ge \beta_{b,\max} , \\ \dfrac{1}{qS_{\rm obs}} \dfrac{(1-\cos^2\theta)^{-a-1}}{(1-\beta_{b,\max})^{-a-1}-1}\, dS_{\rm obs} , & \cos\theta \le \beta_{b,\max} . \end{cases} \tag{A19}$$

For the inversion, analogous to equation (A12), the denominator, or normalization factor, which we will call N, has an integral which can be performed numerically for any given value of $a > 0$:

$$N \equiv (1-\beta_{b,\max}^2)^{-a} - (1-\beta_{b,\max})^{-a} + a\beta_{b,\max} \int_{\cos\theta=0}^{\cos\theta=\beta_{b,\max}} d(\cos\theta)(1-\cos^2\theta)^{-a-1} . \tag{A20}$$

Thus

$$p(\theta)d\theta = \begin{cases} \dfrac{a\beta_{b,\max}}{N}(1-\beta_{b,\max}\cos\theta)^{-a-1}\sin\theta\, d\theta , & \cos\theta \ge \beta_{b,\max} , \\ \dfrac{a\beta_{b,\max}}{N}(1-\cos^2\theta)^{-a-1}\sin\theta\, d\theta , & \cos\theta \le \beta_{b,\max} , \end{cases} \tag{A21}$$

which is independent of $S_{\rm obs}$, as in case II. With equation (A2) it then follows that

$$P(\beta'_{\rm app} \le \beta_{\rm app}) = 1 - \frac{1}{N}\left[(1-\beta_{b,\max}^2)^{-a} - \left(\frac{1-D_m}{\beta_{\rm app}^2+1}\right)^{-a} + a\beta_{b,m}\int_{\cos\theta=\xi}^{\cos\theta=\beta_{b,\max}} d(\cos\theta)(1-\cos^2\theta)^{-a-1}\right], \tag{A22}$$

where $\xi = \beta_{\rm app}(\beta_{\rm app}^2+1)^{-1/2}$. The integral in equation (A22) can again be performed numerically for any $a > 0$.

REFERENCES

Abramowicz, M. A. 1992, in Extragalactic Radio Sources: From Beams to Jets, ed. J. Roland, H. Sol, & G. Pelletier (Cambridge: Cambridge Univ. Press), 206
Akujor, C. E. 1992, A&A, 259, L61
Alberdi, A., et al. 1993, A&A, 271, 93
Alef, W., Götz, M. M. A., Preuss, E., & Kellermann, K. I. 1988, A&A, 192, 53
Antonucci, R. R. J., Hickson, P., Miller, J. S., & Olszewski, E. W. 1987, AJ, 92, 1
Antonucci, R. R. J., & Ulvestad, J. S. 1985, ApJ, 294, 158
Bååth, L. B. 1984, in IAU Symp. 110, VLBI and Compact Radio Sources, ed. R. Fanti, K. Kellermann, & G. Setti (Dordrecht: Reidel), 127
———. 1987, in Superluminal Radio Sources, ed J. A. Zensus & T. J. Pearson (Cambridge: Cambridge Univ. Press), 206
Bååth, L. B., & Zhang, F. J. 1991, A&A, 243, 328
Bååth, L. B., et al. 1980, A&A, 86, 364
Bååth, L. B., Zhang, F. J., & Chu, H. S. 1991, A&A, 250, 50
Bartel, N., Herring, T. A., Ratner, M. I., Shapiro, I. I., & Corey, B. E. 1986, Nature, 319, 733
Barthel, P. D. 1989, ApJ, 336, 606
Barthel, P. D., Miley, G. K., Schilizzi, R. T., & Preuss, E. 1984, A&A, 140, 399
Barthel, P. D., Pearson, T. J., Readhead, A. C. S., & Canzian, B. J. 1986, ApJ, 310, L7
Barthel, P. D., Hooimeyer, J. R. A., Schilizzi, R. T., Miley, G. K., & Preuss, E. 1989, ApJ, 336, 601
Baum, S. A., O'Dea, C. P., Murphy, D. W., & de Bruyn, A. G. 1990, A&A, 232, 19
Bicknell, G. V. 1994, ApJ, 422, 542
Biretta, J. A., Moore, R. L., & Cohen, M. H. 1986, ApJ, 308, 93
Blandford, R. D. 1990, in Saas-Fée Advanced Course 20 Lecture Notes, Active Galactic Nuclei, ed. T. J.-L. Courvoisier & M. Mayor (Berlin: Springer), 239
Briggs, F. H., Wolfe, A. M., Liszt, H. S., Davis, M. M., & Turner, K. L. 1989, ApJ, 341, 650
Browne, I. W. A. 1987, in Superluminal Radio Sources, ed. J. A. Zensus & T. J. Pearson (Cambridge: Cambridge Univ. Press), 129
Browne, I. W. A., & Perley, R. A. 1986, MNRAS, 222, 149
Burbidge, E. M., & Kinman, T. D. 1966, ApJ, 145, 654
Burbidge, E. M., & Rosenberg, F. D. 1965, ApJ, 142, 1673
Burbidge, E. M., & Strittmatter, P. A. 1972, ApJ, 174, L57
Cawthorne, T. V., Wardle, J. F. C., Roberts, D. H., Gabuzda, D. C., & Brown, L. F. 1993, ApJ, 416, 496
Charlot, P. 1990, A&A, 229, 51
Cohen, M. H. 1989, in BL Lac Objects, ed. L. Maraschi, T. Maccacaro, & M.-H. Ulrich (Berlin: Springer), 13
Cohen, M. H., Barthel, P. D., Pearson, T. J., & Zensus, J. A. 1988, ApJ, 329, 1
Cohen, M. H., & Vermeulen, R. C. 1992, in Extragalactic Radio Sources: From Beams to Jets, ed. J. Roland, H. Sol, & G. Pelletier (Cambridge: Cambridge Univ. Press), 98
Cohen, M. H., Zensus, J. A., Biretta, J. A., Comoretto, G., Kaufmann, P., & Abraham, Z. 1987, ApJ, 315, L89
Conway, J. E., & Murphy, D. W. 1993, ApJ, 411, 89
Conway, J. E., Pearson, T. J., Readhead, A. C. S., Unwin, S. C., Xu, W., & Mutel, R. L. 1992, ApJ, 396, 62
Conway, J. E., Unwin, S. C., Pearson, T. J., Readhead, A. C. S., & Xu, W. 1990, in Compact Steep-Spectrum and GHz-peaked Spectrum Radio Sources, ed. C. Fanti, R. Fanti, C. P. O'Dea, & R. T. Schilizzi (Bologna: CNR Istituto di Radioastronomia), 157
Cotton, W. D., et al. 1979, ApJ, 229, L115
Dallacasa, D., & Stanghellini, C. 1990, in Compact Steep-Spectrum and GHz-peaked Spectrum Radio Sources, ed. C. Fanti, R. Fanti, C. P. O'Dea, & R. T. Schilizzi (Bologna: CNR Istituto di Radioastronomia), 224
Ekers, R. D., & Liang, H. 1990, in Parsec-Scale Radio Jets, ed. J. A. Zensus & T. J. Pearson (Cambridge: Cambridge Univ. Press), 333
Gabuzda, D. C., Cawthorne, T. V., Roberts, D. H., & Wardle, J. F. C. 1989a, ApJ, 347, 701
Gabuzda, D. C., Kollgaard, R. I., Roberts, D. H., & Wardle, J. F. C. 1993, ApJ, 410, 39
Gabuzda, D. C., Wardle, J. F. C., & Roberts, D. H. 1989b, ApJ, 336, L59
Ghisellini, G., Padovani, P., Celotti, A., & Maraschi, L. 1993, ApJ, 407, 65
Glassgold, A. E., et al. 1983, ApJ, 274, 101
Gregory, P. C., & Condon, J. J. 1991, ApJS, 75, 1011
Henri, G., & Pelletier, G. 1992, in Extragalactic Radio Sources: From Beams to Jets, ed. J. Roland, H. Sol, & G. Pelletier (Cambridge: Cambridge Univ. Press), 221
Herbig, T., & Readhead, A. C. S. 1992, ApJS, 81, 83
Hewitt, A., & Burbidge, G. 1991, ApJS, 75, 297

Hooimeyer, J. R. A., Barthel, P. D., Schilizzi, R. T., & Miley, G. K. 1992a, A&A, 261, 1
———. 1992b, A&A, 261, 18
Hooimeyer, J. R. A., Schilizzi, R. T., Miley, G. K., & Barthel, P. D. 1992c, A&A, 261, 5
Hough, D. H., & Readhead, A. C. S. 1987, ApJ, 321, L11
———. 1989, AJ, 98, 1208
Hough, D. H., Readhead, A. C. S., Wood, D. A., & Feldmeier, J. J. 1992, ApJ, 393, 81
Hough, D. H., Zensus, J. A., Vermeulen, R. C., Readhead, A. C. S., Porcas, R. W., & Rius, A. 1993, in Subarcsecond Radio Astronomy, ed. R. J. Davis, & R. S. Booth (Cambridge: Cambridge Univ. Press), 195
Hummel, C. A., et al. 1992, A&A, 257, 489
Impey, C. D., Lawrence, C. R., & Tapia, S. 1991, ApJ, 375, 46
Jones, D. L. 1986, ApJ, 309, 5
Jones, T. W. 1988, ApJ, 332, 678
Kapahi, V. K. 1987, in IAU Symp. 124, Observational Cosmology, ed. A. Hewitt, G. Burbidge, & L. Z. Fang (Dordrecht: Reidel), 251
Kapahi, V. K., & Murphy, D. W. 1990, in Parsec-Scale Radio Jets, ed. J. A. Zensus & T. J. Pearson (Cambridge: Cambridge Univ. Press), 313
Kellermann, K. I. 1993, Nature, 361, 134
Kollgaard, R. I., Wardle, J. F., & Roberts, D. H. 1990, AJ, 100, 1057
Krichbaum, T. P., Hummel, C. A., Quirrenbach, A., Schalinski, C. J., Witzel, A., Johnston, K. J., Muxlow, T. W. B., & Qian, S. J. 1990a, A&A, 230, 271
Krichbaum, T. P., et al. 1990b, A&A, 237, 3
Kühr, H., Witzel, A., Pauliny-Toth, I. I. K., & Nauber, U. 1981, A&AS, 45, 367
Kus, A. J., Wilkinson, P. N., Pearson, T. J., & Readhead, A. C. S. 1990, in Parsec-Scale Radio Jets, ed. J. A. Zensus & T. J. Pearson (Cambridge: Cambridge Univ. Press), 161
Lind, K. 1987, in Superluminal Radio Sources, ed. J. A. Zensus & T. J. Pearson (Cambridge: Cambridge Univ. Press), 180
Lind, K., & Blandford, R. D. 1985, ApJ, 295, 358
Lynden-Bell, D. 1977, Nature, 270, 396
Lynds, C. R. 1967, ApJ, 147, 837
Lynds, C. R., Stockton, A. N., & Livingston, W. C. 1965, ApJ, 142, 1667
Marcaide, J. M., Alberdi, A., Elosegui, P., Schalinski, C. J., Jackson, N., & Witzel, A. 1989, A&A, 211, L23
Marr, J. M., Backer, D. C., & Wright, M. C. H. 1990, in Parsec-Scale Radio Jets, ed. J. A. Zensus & T. J. Pearson (Cambridge: Cambridge Univ. Press), 78
Marscher, A. P., & Broderick, J. J. 1985, ApJ, 290, 735
McHardy, I. M., Marscher, A. P., Gear, W. K., Muxlow, T., Letho, H. J., & Abraham, R. G. 1993, MNRAS, 261, 464
Meier, D. L., et al. 1993, in Subarcsecond Radio Astronomy, ed. R. J. Davis & R. S. Booth (Cambridge: Cambridge Univ. Press), 201
Murphy, D. W. 1990, in Parsec-Scale Radio Jets, ed. J. A. Zensus & T. J. Pearson (Cambridge: Cambridge Univ. Press), 298
Mutel, R. L. 1990, in Parsec-Scale Radio Jets, ed. J. A. Zensus & T. J. Pearson (Cambridge: Cambridge Univ. Press), 98
Mutel, R. L., Phillips, R. B., Su, B., & Bucciferro, R. R. 1990, ApJ, 352, 81
O'Dea, C. P., Baum, S. A., & Stanghellini, C. 1991, ApJ, 380, 66
Orr, M. J. L., & Browne, I. W. A. 1982, MNRAS, 200, 1067
Owen, F. N., & Puschell, J. J. 1984, AJ, 89, 932
Padovani, P. 1992, A&A, 256, 399
Padovani, P., & Urry, C. M. 1992, ApJ, 387, 449
Pauliny-Toth, I. I. K., Porcas, R. W., Zensus, J. A., Kellermann, K. I., Wu, S. Y., Nicholson, G. D., & Mantovani, F. 1987, Nature, 328, 778
Pauliny-Toth, I. I. K., Zensus, J. A., Cohen, M. H., Alberdi, A., & Schaal, R. 1990, in Parsec-Scale Radio Jets, ed. J. A. Zensus & T. J. Pearson (Cambridge: Cambridge Univ. Press), 55
Pearson, T. J., Barthel, P. D., Lawrence, C. R., & Readhead, A. C. S. 1986, ApJ, 300, L25
Pearson, T. J., & Readhead, A. C. S. 1988, ApJ, 328, 114
Pearson, T. J., & Zensus, J. A. 1987, in Superluminal Radio Sources, ed. J. A. Zensus & T. J. Pearson (Cambridge: Cambridge Univ. Press), 1
Pedlar, A., Ghataure, H. S., Davies, R. D., Harrison, B. A., Perley, R., Crane, P. C., & Unger, S. W. 1990, MNRAS, 246, 477
Pelletier, G., & Roland, J. 1989, A&A, 224, 24
———. 1990, in Parsec-Scale Radio Jets, ed. J. A. Zensus & T. J. Pearson (Cambridge: Cambridge Univ. Press), 323
Phillips, M. M. 1977, ApJ, 215, 746
Phinney, E. S. 1987, in Superluminal Radio Sources, ed. J. A. Zensus & T. J. Pearson (Cambridge: Cambridge Univ. Press), 301
Polatidis, A. G., Wilkinson, P. N., & Akujor, C. E. 1993, in Subarcsecond Radio Astronomy, ed. R. J. Davis & R. S. Booth (Cambridge: Cambridge Univ. Press), 225
Porcas, R. W. 1981, Nature 294, 47
———. 1987, in Superluminal Radio Sources, ed. J. A. Zensus & T. J. Pearson (Cambridge: Cambridge Univ. Press), 12
———. 1990, in Compact Steep-Spectrum and GHz-peaked Spectrum Radio Sources, ed. C. Fanti, R. Fanti, C. P. O'Dea, & R. T. Schilizzi (Bologna: CNR Istituto di Radioastronomia), 167
Preuss, E. 1983, in Astrophysical Jets, ed. A. Ferrari & A. G. Pacholczyk (Dordrecht: Reidel), 1
Preuss, E., Alef, W., Shengyin, W., Yuhai, Q., Zhihan, Q., Kellermann, K. I., Matveenko, L., & Götz, M. M. A. 1990, in Parsec-Scale Radio Jets, ed. J. A. Zensus & T. J. Pearson (Cambridge: Cambridge Univ. Press), 120
Quirrenbach, A., et al. 1992, A&A, 258, 279
Readhead, A. C. S. 1994, ApJ, 426, 51
Readhead, A. C. S., Pearson, T. J., & Unwin, S. C. 1984, in VLBI and Compact Radio Sources, Proc. IAU Symp. 110, ed. R. Fanti, K. Kellermann, & G. Setti (Dordrecht: Reidel), 131
Readhead, A. C. S., Xu, W., Pearson, T. J., Wilkinson, P., & Polatidis, A. 1993, BAAS, 25, 891
Reid, M. J., Biretta, J. A., Junor, W., Muxlow, T. W. B., & Spencer, R. E. 1989, ApJ, 336, 112
Richstone, D. O., & Schmidt, M. 1980, ApJ, 235, 361
Roland, J., Charlot, P., Lestrade, J.-F., Miley, G., Pelletier, G., & Schilizzi, R. 1993, Class. Quantum Grav. 10, S251
Rust, B. W., Nash, S. G., & Geldzahler, B. J. 1989, Ap&SS, 152, 141
Sargent, W. L. W. 1977, ApJ, 212, L105
Schalinski, C. J. 1990, Ph.D. thesis, Bonn Univ.
Schalinski, C. J., Alberdi, A., Elósegui, P., & Marcaide, J. M. 1988, in IAU Symp. 129, The Impact of VLBI on Astrophysics and Geophysics, ed. M. J. Reid & J. M. Moran (Dordrecht: Kluwer), 39
Schalinski, C. J., Witzel, A., Hummel, C. A., Krichbaum, T. P., Quirrenbach, A., & Johnston, K. J. 1992, in Variability of Blazars, ed. E. Valtaoja & M. Valtonen (Cambridge: Cambridge Univ. Press), 225
Scheuer, P. A. G. 1987, in Superluminal Radio Sources, ed. J. A. Zensus & T. J. Pearson (Cambridge: Cambridge Univ. Press), 104
Scheuer, P. A. G., & Readhead, A. C. S. 1979, Nature, 277 182
Shaffer, D. B., Marscher, A. P., Marcaide, J., & Romney, J. D. 1987, ApJ, 314, L1
Simon, R. S., Hall, J., Johnston, K. J., Spencer, J. H., Waak, J. A., & Mutel, R. L. 1988a, ApJ, 326, L5
Simon, R. S., Johnston, K. J., & Spencer, J. H. 1985, ApJ, 290, 66
———. 1988b, in IAU Symp. 129, The Impact of VLBI on Astrophysics and Geophysics, ed. M. J. Reid & J. M. Moran (Dordrecht: Kluwer), 21
Stanghellini, C., O'Dea, C. P., Baum, S. A., & Fanti, R. 1990, in Compact Steep-Spectrum and GHz-peaked Spectrum Radio Sources, ed. C. Fanti, R. Fanti, C. P. O'Dea, & R. T. Schilizzi (Bologna: CNR Istituto di Radioastronomia), 17
Stickel, M., Fried, J. W., & Kühr, H. 1989, A&AS, 80, 103
Stickel, M., & Kühr, H. 1993, A&AS, 100, 395
Stickel, M., Padovani, P., Urry, C. M., Fried, J. W., & Kühr, H. 1991, ApJ, 374, 431
Turland, B. D. 1975, MNRAS, 170, 281
Tzioumis, A. K., et al. 1990, AJ, 98, 36
Ulvestad, J. S., Johnston, K. J., Perley, R. A., & Fomalont, E. B. 1981, AJ, 86, 1010
Unwin, S. C., Cohen, M. H., Biretta, J. A., Hodges, M. W., & Zensus, J. A. 1989, ApJ, 340, 117
Unwin, S. C., Cohen, M. H., Biretta, J. A., Pearson, T. J., Seielstad, G. A., Walker, R. C., Simon, R. S., & Linfield, R. P. 1985, ApJ, 289, 109
Urry, C. M., & Padovani, P. 1991, ApJ, 371, 60
Urry, C. M., Padovani, P., & Stickel, M. 1991, ApJ, 382, 501
Urry, C. M., & Shafer, R. A. 1984, ApJ, 280, 569
van Breugel, W. J. M., Fanti, C., Fanti, R., Stanghellini, C., Schilizzi, R. T., & Spencer, R. E. 1992, A&A, 256, 56
Venturi, T., Giovannini, G., Feretti, L., Comoretto, G., & Wehrle, A. E. 1993a, ApJ, 408, 81
Venturi, T., Pearson, T. J., Barthel, P. D., & Herbig, T. 1993b, A&A, 271, 65
Vermeulen, R. C., Bernstein, R. A., Hough, D. H., & Readhead, A. C. S. 1993, ApJ, 417, 541
Vermeulen, R. C., & Cohen, M. H. 1994, in preparation
Véron-Cetty, M. P., & Véron, P. 1991, ESO Scientific Repo. No. 10
Waggett, P. C., Warner, P. J., & Baldwin, J. E. 1977, MNRAS, 181, 465
Walker, R. C., Benson, J. M., & Unwin, S. C. 1987, in Superluminal Radio Sources, ed. J. A. Zensus, & T. J. Pearson (Cambridge: Cambridge Univ. Press), 48
Wehrle, A. E., & Cohen, M. H. 1989, ApJ, 346, L69
Wehrle, A. E., Cohen, M. H., & Unwin, S. C. 1990, ApJ, 351, L1
Wilkinson, P. N., Tzioumis, A. K., Akujor, C. E., Benson, J. M., Walker, R. C., & Simon, R. S. 1990, in Parsec-Scale Radio Jets, ed. J. A. Zensus & T. J. Pearson (Cambridge: Cambridge Univ. Press), 152
Wills, B. J., et al. 1983, ApJ, 274, 62
Witzel, A., Schalinski, C. J., Johnston, K. J., Biermann, P. L., Krichbaum, T. P., Hummel, C. A., & Eckart, A. 1988, A&A, 206, 245
Yahil, A. 1979, ApJ, 233, 775
Zensus, J. A. 1991, in Frontiers of VLBI, ed. H. Hirabayashi, M. Inoue, & H. Kobayashi (Tokyo: Universal Academy Press), 319
Zensus, J. A., & Pearson, T. J. 1988, in IAU Symp. 129, The Impact of VLBI on Astrophysics and Geophysics, ed. M. J. Reid & J. M. Moran (Dordrecht: Kluwer), 7
Zensus, J. A., & Porcas, R. W. 1987, in Superluminal Radio Sources, ed. J. A. Zensus & T. J. Pearson (Cambridge: Cambridge Univ. Press), 126
Zensus, J. A., Hough, D. H., & Porcas, R. W. 1987, Nature, 325, 36
Zensus, J. A., Bååth, L. B., Cohen, M. H., & Nicholson, G. D. 1988, Nature, 334, 410
Zensus, J. A., Unwin, S. C., Cohen, M. H., & Biretta, J. A. 1990, AJ, 100, 1777
Zensus, J. A., Cohen, M. H., & Unwin, S. C. 1994, in preparation
Zhang, F. J., & Bååth, L. B. 1990, A&A, 236, 47